

SANS investigation of fungal loosenins reveal substrate dependent impacts of protein 1 action on inter-fibril distance and packing order of cellulosic substrates

Deepika Dahiya

Aalto University

Zsuzsanna Péter-Szabó

KTH Royal Institute of Technology

Manjula Senanayake

Oak Ridge National Laboratory

Sai Venkatesh Pingali

Oak Ridge National Laboratory

Wellington C. Leite

Oak Ridge National Laboratory

James Byrnes

Brookhaven National Laboratory

Garry W. Buchko

Pacific Northwest National Laboratory

Pramod Sivan

KTH Royal Institute of Technology

Francisco Vilaplana

KTH Royal Institute of Technology

Emma Master

emma.master@utoronto.ca

University of Toronto

Hugh O'Neill

Oak Ridge National Laboratory

Research Article

Keywords: expansin, loosenin, lignocellulose, small-angle neutron scattering, solution NMR structure

Posted Date: August 14th, 2024

DOI: <https://doi.org/10.21203/rs.3.rs-4769386/v1>

License:  This work is licensed under a Creative Commons Attribution 4.0 International License.

[Read Full License](#)

Additional Declarations: No competing interests reported.

1 **SANS investigation of fungal loosening reveal substrate dependent impacts of protein**
2 **action on inter-fibril distance and packing order of cellulosic substrates**

3
4 Deepika Dahiya¹, Zsuzsanna Péter-Szabó², Manjula Senanayake⁴, Sai Venkatesh Pingali⁴,
5 Wellington C. Leite⁴, James Byrnes⁵, Garry W. Buchko⁶, Pramod Sivan², Francisco Vilaplana^{2,3},
6 Emma R. Master^{1,7*}, Hugh O'Neill^{4*}

7
8 ¹Department of Bioproducts and Biosystems, Aalto University, Kemistintie 1, 02150 Espoo,
9 Finland.

10 ²Division of Glycoscience, Department of Chemistry, KTH Royal Institute of Technology,
11 Stockholm, SE-106 91, Sweden.

12 ³Wallenberg Wood Science Centre, KTH Royal Institute of Technology, Stockholm, SE-100 44,
13 Sweden.

14 ⁴Neutron Scattering Division and Center for Structural Molecular Biology, Oak Ridge National
15 Laboratory, Oak Ridge, TN, 37831, USA.

16 ⁵Brookhaven National Laboratory, National Synchrotron Light Source II, Bldg. 745, P.O. Box
17 5000, Upton, NY 11973-5000

18 ⁶Earth and Biological Sciences Directorate, Pacific Northwest National Laboratory, Richland,
19 WA 99354, United States of America; School of Molecular Biosciences, Washington State
20 University, Pullman, WA, 99164, United States of America

21 ⁷Department of Chemical Engineering and Applied Chemistry, University of Toronto, 200
22 College Street, M5S 3E5, Toronto, Ontario, Canada

23 * co-corresponding

24 This manuscript has been coauthored by UT-Battelle, LLC, under Contract No. DE-AC05-
25 00OR22725 with the U.S. Department of Energy. The United States Government retains and the
26 publisher, by accepting the article for publication, acknowledges that the United States
27 Government retains a non-exclusive, paid-up, irrevocable, worldwide license to publish or
28 reproduce the published form of this manuscript or allow others to do so, for United States
29 Government purposes.

30

31 **ABSTRACT**

32 **Background:** Microbial expansin-related proteins include fungal loosening, which have been
33 previously shown to disrupt cellulose networks and enhance the enzymatic conversion of
34 cellulosic substrates. Despite showing beneficial impacts to cellulose processing, detailed
35 characterization of cellulosic materials after loosening treatment is lacking. In this study, small-
36 angle neutron scattering (SANS) was used to investigate the effects of three recombinantly
37 produced loosening proteins that originate from *Phanerochaete carnosae*, *PcaLOOL7*, *PcaLOOL9*, and
38 *PcaLOOL12*, on the organization of holocellulose preparations from Eucalyptus and Spruce
39 wood samples.

40 **Results:** Whereas the SANS analysis of Spruce holocellulose revealed an increase in interfibril
41 spacing of neighboring cellulose microfibrils following treatment with *PcaLOOL12* and to a
42 lesser extent *PcaLOOL7*, the analysis of Eucalyptus holocellulose revealed a reduction in
43 packing number following treatment with *PcaLOOL12* and to a lesser extent *PcaLOOL9*.
44 Parallel SEC-SAXS characterization of *PcaLOOL7*, *PcaLOOL9*, and *PcaLOOL12* indicated the
45 proteins likely function as monomers; moreover, all appear to retain a flexible disordered N-
46 terminus and folded C-terminal region. The comparatively high impact of *PcaLOOL12*

47 motivated its NMR structural characterization, revealing a double-*psi* β -barrel (DPBB) domain
48 surrounded by three α -helices - the largest nestled against the DPBB core and the other two part
49 of loops extending from the core.

50 **Conclusions:** The SANS analysis of *Pca*LOOL action on holocellulose samples confirms their
51 ability to disrupt cellulose fiber networks and suggests a progression from reducing microfibril
52 packing to increasing interfibril distance. The most impactful *Pca*LOOL, *Pca*LOOL12, was
53 previously observed to be the most highly expressed loosenin in *P. carnosus*. Its structural
54 characterization herein reveals its stabilization through two disulfide linkages, and an extended
55 N-terminal region distal to a negatively charged and surface accessible polysaccharide binding
56 groove.

57

58

59 **Keywords:** expansin, loosenin, lignocellulose, small-angle neutron scattering, solution NMR
60 structure

61

62

63

64

65

66

67

68

69

70 **BACKGROUND**

71 Expansins are an intriguing group of plant proteins that induce plant cell loosening through
72 promoting cell wall creep and stress relaxation at acidic pH (1–3). Although the molecular
73 mechanism of expansins is not fully understood, all expansins characterized to date lack
74 detectable lytic activity. Instead, these proteins are thought to physically disrupt non-covalent
75 interactions between cellulose and matrix polysaccharides (e.g., pectin, hemicelluloses),
76 potentially at distinctive and limited locations characterized by tight junctions between
77 neighboring cellulose microfibrils (4,5).

78
79 Over the past decade, genome sequencing has uncovered the prevalence of expansin-like
80 proteins in microorganisms, including bacteria and fungi (6–9). Both plant expansins and
81 microbial expansin-like proteins (EXLX) exhibit a two-domain structure comprising an N-
82 terminal six-stranded double-*psi* b-barrel domain (D1) resembling glycoside hydrolases from
83 family 45 (GH45) although lacking all requisite catalytic amino acids. The D1 domain is
84 connected through a short linker to a C-terminal domain (D2) that adopts a fold similar to group
85 2 grass pollen allergens and is classified as a family-63 carbohydrate binding module (CBM63)
86 (10). The comparative ease to recombinantly produce microbial EXLX proteins, such as
87 *BsEXLX1* from *Bacillus subtilis*, has advanced sequence-functional characterizations of the
88 expansin protein family (10–12). For example, structural and mutagenesis studies of *BsEXLX1*
89 confirm the critical importance of Asp82 in the D1 domain to protein function, as well as the
90 importance of aromatic amino acids in the D2 domain, including Trp125 and Trp126, to
91 cellulose binding (11).

92

93 Besides EXLX proteins, the broader set of microbial expansin-related proteins include loosenins
94 and ceratoplatanins that retain only the D1 domain of EXLXs, and swollenins that comprise an
95 N-terminal family-1 CBM and fibronectin domain in addition to the core EXLX structure (13-
96 15). Notably, the swollenin *TrSWO1* from *Trichoderma reesei* exhibits low hydrolytic activity
97 towards soluble cello-oligosaccharides (16), which might be explained by the several insertions
98 and deletions in the D1 domain that differentiate swollenins from other expansin-related proteins
99 (17).

100

101 So far, most studies of microbial expansin-related proteins have investigated their potential to
102 boost enzymatic hydrolysis of lignocellulosic substrates (17–21). Overall, the impact of
103 microbial expansin-related proteins on the enzymatic deconstruction of lignocellulose varies and
104 depends on the lignocellulose source, enzyme cocktail, and enzyme dose (22,23). Different
105 biophysical methods have also been used to study the impact of microbial expansins on the
106 structure of cellulose fibers. For example, studies using light microscopy show treatment of
107 mercerized cotton fiber with *TrSWO1* induces fiber swelling (15). On the other hand, subsequent
108 studies using scanning electron microscopy and atomic force microscopy show that treatment of
109 cellulosic material with *TrSWO1* leads to smoother fiber surfaces (24). Nevertheless, *TrSWO1*
110 reduces the tensile strength of filter paper (15) as has been similarly reported for several
111 microbial expansin-like proteins such as *BsEXLX1*(11), *HcEXLX2* from *Hahella chejuensis*
112 (25), *PcEx11* from *Pectobacterium carotovorum* (26), and loosenins including *LOOS1* from
113 *Bjerkandera adusta* (14) and *PcaLOOLs* from *Phanerochaete carnososa* (27). Clearly, additional
114 and direct comparisons of multiple expansin-related proteins on defined lignocellulosic

115 substrates are needed to elucidate their mode of action and substantiate sequence and substrate
116 dependent impacts on protein function.
117

118 Small-angle neutron scattering (SANS) is a powerful approach to characterizing the morphology
119 and organization of a wide variety of complex materials (28). In particular, it has been used to
120 characterize plant cell wall structure under a variety of conditions providing nanoscale
121 information about cell wall organization. For instance, it can simultaneously measure changes in
122 intra-fibrillar (e.g., swelling) and inter-fibrillar (e.g., organization) cellulose fiber structures (29).
123 Moreover, because SANS is a non-destructive analysis method, biological samples can be
124 recovered for parallel investigations. SANS was previously used to investigate the impact of
125 cellulolytic enzymes and chelator-mediated Fenton (CMF) chemistry on southern yellow pine
126 and revealed an increase in inter-fibril spacing following CMF treatment that was enhanced
127 when treating delignified wood fiber (30). Here, SANS is used to compare the action of three
128 loosenins from *P. carnosus* (*PcaLOOL7*, *PcaLOOL9*, and *PcaLOOL12*) on wood holocellulose
129 fibers, i.e. cellulosic fibers that have been partially delignified but retain most of the
130 hemicellulose populations, from two representative wood sources (Spruce softwoods and
131 Eucalyptus hardwoods) with distinct lignin and hemicellulose compositions. The selected
132 *PcaLOOLs* were previously shown to weaken filter paper, reduce yield strain of cellulose
133 nanofibers, and improve cellulolytic conversion of complex lignocellulosic substrates including
134 steam pretreated softwood and hardwood and softwood kraft pulps (21,27). The current SANS
135 analyses of these proteins deepen our understanding of their mode of action, thereby shedding
136 light on the biological relevance of this protein family and their application in biomass
137 processing.

138

139 **METHODS**

140 **Materials.** Wood chips from softwood Spruce *Picea abies* and hardwood *Eucalyptus grandis*
141 were provided by UPM-Kymene Oyj (Helsinki, Finland) and were used to prepare substrate
142 specimens for protein treatment. The wood chips were cut to a matchstick size (approximately 2
143 mm in the tangential x 1 mm in radial x 20 mm in the longitudinal direction of the wood section).
144 Before delignification, low molecular weight wood extractives and resins were removed
145 according to the SCAN-CM 49:03 standard procedure. Acetone Soxhlet extraction was carried
146 out for 6 h, during which time the spent solvent was replaced with fresh solvent every hour.

147

148 **Holocellulose preparation and characterization.** Acetone extracted wood sections (1 g) were
149 mixed in 15 mL deionized water using magnetic stirrer and heated to 75 °C. Glacial acetic acid
150 (0.1 mL) and 0.3 g NaClO₂ per g of wood section were then added every hour for 6 h (31,32).

151

152 For total carbohydrate analysis, freeze dried native and holocellulose wood samples were
153 incubated with concentrated 72 w/w% sulfuric acid at 8 mg/mL for 3 h at room temperature. The
154 samples were then diluted to 0.67 mg/mL with Milli-Q water and hydrolyzed at 100 °C for 3 h
155 (33). Parallel treatments were performed to quantify both the neutral monosaccharides and
156 uronic acids of the non-cellulosic polysaccharides in the wood and the holocellulose samples by
157 trifluoroacetic acid (TFA) hydrolysis. Briefly, 1 mg of the solid samples were hydrolyzed at 1
158 mg/mL in 2 M trifluoroacetic acid (TFA) for 3 h at 120 °C, dried under airflow, and dissolved in 1
159 mL Milli-Q water. The resulting monosaccharides from both sulfuric and TFA hydrolyses were
160 then quantified using high-performance anion-exchange chromatography coupled with pulsed

161 amperometric detection (HPAEC-PAD)(34). The HPAEC-PAD analysis was performed using a
162 Dionex ICS-6000 system (Thermo Fischer, MA, USA) equipped with a CarboPac PA20 (3 × 150
163 mm) column. The eluents for chromatography were Milli-Q water (eluent A), 200 mM NaOH
164 (eluent B), and 100 mM sodium acetate in 100 mM NaOH (eluent C) at a flow rate of 0.4
165 mL/min. The neutral sugars were separated over 18 min in 98.8 % eluent A and 1.2 % eluent B
166 (2.4 mM NaOH). The column was then equilibrated with 50 % eluent A and 50 % eluent B for
167 10 min, and the uronic acids were further eluted over 16 min at 100 % eluent C. The
168 quantification of each monosaccharide was performed using calibration curves of neutral sugars
169 and uronic acid standards (fucose, arabinose, rhamnose, glucose, xylose, mannose, galacturonic
170 acid, glucuronic acid, and 4-*O*-methyl-glucuronic acid).

171
172 The total lignin content of the initial wood samples was determined using the acetyl bromide
173 method (35,36) with modifications to prevent xylan degradation, which can interfere with lignin
174 quantification (37). Briefly, 5 mg of freeze-dried and ball milled wood powder was weighed and
175 digested with 1 mL 25 v/v % acetyl bromide in glacial acetic acid solution for 2 h at 50 °C.
176 Samples were cooled on ice and diluted with 5 mL glacial acetic acid; 90 µL of the diluted
177 sample were then mixed with 120 µL of 2 M NaOH and 90 µL 0.5 M hydroxylamine
178 hydrochloride solution to achieve a 3:4:3 volumetric ratio of sample: 2M NaOH: 0.5M
179 hydroxylamine hydrochloride. Absorbance was measured at 280 nm using a BMG Labtech
180 CLARIOstar spectrophotometer (BMG Labtech, Ortenberg, Germany). Calculations of lignin
181 concentration were performed using a calibration curve of acetyl bromide digested alkali lignin.

182

183 **Recombinant production and purification.** Three loosenins from *Phanerochaete carnos*
184 (*Pca*LOOL7 (GenBank code EKM53490.1), *Pca*LOOL9 (GenBank code EKM52742.1) and
185 *Pca*LOOL12 (GenBank code EKM51974.1) were recombinantly produced with a C-terminal
186 His₆-tag in *Pichia pastoris* SMD1168H according to the Pichia fermentation guidelines and
187 using a 7 L Sterilizable-In-Place (SIP) Fermenter (BIOSTAT® Cplus bioreactor, Sartorius,
188 Göttingen, Germany) fitted with pH (Article no. BB-34090812), oxygen (Article no. BB-
189 8848663) and turbidity HAMILTON probes from Sartorius (21, 27). Precultures for the
190 bioreactor were prepared by transferring fresh colonies of each transformant from YPD agar
191 plates (supplemented with zeocin) into 300 mL BMGY (Buffered Glycerol-complex Medium)
192 and growing the cultures at 30 °C and 180 rpm for 16-24 h until the OD_{600nm} reached between
193 20-25. The pre-culture medium was replaced with 50 mL of sterile minimal basal salts medium
194 (BSM) before transferring the cells to the bioreactor containing sterilized 3.5 L BSM media
195 containing 4 % (w/v) glycerol and 0.4 % (v/v) PTM1 fermentation trace salts (VWR, PA, USA).
196 The reactor was supplemented with approximately 100 µL of antifoaming agent Struktol J 647 to
197 prevent the formation of foam throughout the fermentation. The glycerol growth phase was
198 performed at 30 °C and pH 6.0. The maximum stirring rate was set to 900 rpm, air flow rate to
199 40-60 %, volume of air per volume of liquid per minute (VVM) between 0.5-1.0, and the oxygen
200 level was set to 35 %. The oxygen was maintained by using automatic cascade with stirring and
201 gas flow until the cells approached the stationary phase, at which time the Glycerol Fed-Batch
202 Phase was initiated with up to 4 % w/v of glycerol feeding for over 5 to 6 h to achieve higher cell
203 density. To induce recombinant protein production, the temperature was lowered to 20 °C and
204 methanol was added at up to 6.5 mL/ h/ L of media for up to 110 h.
205

206 Following induction, the pH of the culture was increased to pH 7.8 using 4 M NaOH before
207 removing the cells by centrifugation and filtering the culture supernatant through a 0.45 µm
208 polyethersulfone (PES) filter (Millipore). The recombinant *Pca*LOOLs were then purified by
209 affinity chromatograph using Ni-NTA resin as previously described (27). The purified protein
210 was exchanged to 20 mM sodium acetate (pH 6.0) and concentrated to 10-15 mg/mL using
211 Vivaspin® 20 Ultrafiltration Units (5 kDa and 10 kDa) from Sartorius before flash-freezing and
212 storage at -80 °C. The protein purity was verified by SDS-PAGE and protein concentration was
213 determined by absorbance at 280 nm using a Thermofischer Scientific NanoDrop™ Lite
214 Spectrophotometer (Thermo, Fischer, MA, USA).

215

216 To prepare recombinant protein for NMR studies, an oligonucleotide sequence for *Pca*LOOL12,
217 with the predicted 19-residue N-terminal signal sequence replaced with a polyhistidine affinity
218 tag (bold) and a TEV protease cleave site (underlined), (MGSS**HHHHHHH**SSGENLYFQGH-),
219 was synthesized by Genscript (Piscataway, NJ, USA) and inserted into the pET-32a(+)
220 expression vector at the MscI/HindIII restriction enzyme sites such that the expressed protein
221 was fused to thioredoxin (109-residues) at the N-terminal (Trx-*Pca*LOOL12). Fusion of
222 *Pca*LOOL12 to thioredoxin moiety was necessary to improve the expression of soluble
223 *Pca*LOOL12 (no soluble expression observed in constructs without the thioredoxin tag) (38, 39).
224 This recombinant plasmid was then used to transform chemically competent *Escherichia coli*
225 BL21(DE3) cells (Novagen, Darmstadt, Germany) using a heat-shock method. Single colonies
226 from streaked LB-agar plates supplemented with the antibiotic ampicillin (100 mg/mL) were
227 picked, grown to an OD₆₀₀ of ~ 0.8 in 5 to 7 mL of LB medium at 37 °C and used to prepare
228 glycerol frozen stocks (-80 °C) until required. To prepare uniformly ¹⁵N-, ¹³C-labeled Trx-

229 *PcaLOOL12*, 750 mL of minimal medium (Miller) containing $^{15}\text{NH}_4\text{Cl}$ (1 mg/mL), D-
230 $^{13}\text{C}_6$ glucose (2.0 mg/mL), NaCl (50 mg/mL), MgSO_4 (120 mg/mL), CaCl_2 (11 mg/mL), and
231 ampicillin (100 mg/mL) was inoculated directly with 20 mL of LB culture that had grown at 37
232 °C to an OD_{600} of ~ 1. The resulting culture was grown at 37 °C to an OD_{600} ~ 0.8 and then
233 transferred to a 20 °C incubator shaker and protein expression induced overnight with isopropyl
234 β -D-1-thiogalactopyranoside (0.026 mg/mL). Approximately 12 h later the cells were harvested
235 by mild centrifugation and frozen (-80 °C). To make stereospecific assignments of the leucine
236 and valine methyl groups, a 10% ^{13}C -labeled sample was prepared as described above by using
237 D- $^{13}\text{C}_6$ glucose (0.2 mg/mL) and D-glucose (1.8 mg/mL). Following the thawing of a frozen
238 pellet from a 750 mL culture, the cells were lysed using a sonication and French press
239 combination, and the soluble protein was purified with a conventional two-step protocol
240 involving metal chelate affinity chromatography using Ni-NTA resin (GE Healthcare,
241 Piscataway, NJ, USA) followed by gel-filtration chromatography on a Superdex75 HiLoad 26/60
242 column (GE Healthcare, Piscataway, NJ, USA). The latter step exchanged the protein into NMR
243 buffer: 100 mM NaCl, 20 mM Tris, pH 7.0. Following concentration to 1-2 mL, an equal
244 volume of TEV protease buffer (150 mM NaCl, 50 mM TrisHCl, pH 7.8) was added plus 1 μg
245 TEV protease per 100 μg of Trx-*PcaLOOL12*. Following overnight incubation at 4 °C, the
246 digested protein was purified by reapplication to a 5 mL Ni-NTA column. The flow-through and
247 10 mM imidazole fractions were collected, concentrated, and exchanged into NMR buffer to a
248 final concentration of 10 – 15 mg/mL. Note that during the purification process none of the
249 buffers contained reducing agents such as dithiothreitol.
250

251 **NMR data collection for *PcaLOOL12*.** The NMR data for oxidized *PcaLOOL12* was collected
252 at 20 °C on a double-labeled (¹³C-, ¹⁵N-) sample (~ 0.8 mM) using a Varian spectrometer
253 operating at a ¹H resonance frequency of 600 MHz equipped with an HCN-cyproprobe and pulse
254 field gradients. Backbone and side chain chemical shifts (¹H, ¹³C, and ¹⁵N) were assigned from
255 the analysis of two-dimensional ¹H-¹⁵N HSQC, ¹H-¹³C HSQC, HBCBCGCDHD, and
256 HBCBCGCDCHC spectra and three-dimensional HNCACB, CBCA(CO)NH, HNCA, CC-
257 TOCSY-NNH, HNCOC, ¹⁵N-edited NOESY-HSQC, and ¹³C-edited NOESY-HSQC (aliphatic and
258 aromatic) spectra. The NOE data was collected with a mixing time of 90 ms. Backbone
259 hydrogen bonds were made by lyophilizing an ¹⁵N-labeled NMR sample, re-dissolving in a
260 similar volume of 99.8% D₂O, collecting a ¹H-¹⁵N HSQC spectrum (~ 10 min later), and
261 identifying amide resonances that had not yet exchanged with D₂O. The overall rotational
262 correlation time, τ_c , was estimated for oxidized *PcaLOOL12* at 20 °C from the ratio of collective
263 backbone amide ¹⁵N T₁ and T_{1rho} measurements (40). The raw NMR data were processed with
264 NMRpipe (41) and then analyzed with Pocky (42). The ¹H, ¹³C, and ¹⁵N chemical shifts were
265 deposited into the BioMagResBank database (www.bmrb.wisc.edu) with the BMRB number
266 31180.

267
268 **Structure calculations for *PcaLOOL12*.** Assigned ¹H, ¹³C, and ¹⁵N chemical shifts, peak-
269 picked ¹H-¹H NOEs from ¹³C- and ¹⁵N-edited 3D NOESY data sets, and TALOS-derived
270 backbone torsion angles served as initial experimental inputs in iterative structure calculations
271 using the program CYANA (v 2.1) (43). Seventy-five dihedral Psi (Ψ) and Phi (Φ) torsion angle
272 restraints were obtained by the input of the assigned chemical shifts into the program TALOS+
273 using the online webserver (<https://spin.niddk.nih.gov/bax/nmrserver/talos/>) (44). Sixty-eight

274 backbone amide hydrogen bond restraints to backbone carbonyls groups (1.8 – 2.0 Å and 2.7 –
275 3.0 Å for the NH–O and N–O distances, respectively) were introduced into the structure
276 calculation based on consistent proximity in the ensemble and the observation of slowly
277 exchanging amides in the deuterium exchange experiment. Six restraints between the side chain
278 sulfur atoms of C26–C50, and C73–C76 (2.0–2.1 Å, 3.0–3.1 Å, and 3.0–3.1 Å for the S γ –S γ , S γ –
279 C β , and C β –S γ distances, respectively) were introduced into the calculation because of side chain
280 proximity in early structure calculations and cysteine $^{13}\text{C}^\beta$ chemical shifts characteristic of
281 oxidized thiols (Table S1) (45). Towards the end of the calculations, stereo assignments for six
282 leucine and eight valine methyl groups were introduced. The final ensemble of CYANA
283 structures was refined in explicit water (46) using the PARAM19 force-field and force constants
284 of 500, 500, and 1000 kcal for the NOE, hydrogen bond, and dihedral restraints, respectively.
285 For these calculations the upper boundary of all the final CYANA NOE-based distance restraints
286 was increased by 10%. Structural quality was assessed using the online Protein Structure
287 Validation Suite (PSVS, v1.5) (47) with pertinent values included in the structure statistics
288 summary (Table S2). The atomic coordinates for the final ensemble of 20 *PcaLOOL12*
289 structures have been deposited in the Research Collaboratory for Structural Bioinformatics
290 (RCSB) with the PDB ID code 9CE9.

291

292 **Size exclusion chromatography coupled to SAXS of protein samples.** Size exclusion
293 chromatography coupled with small-angle X-ray scattering (SEC-SAXS) was performed at the
294 Life Sciences X-ray Scattering Beamline (LiX) at NSLSII, Brookhaven National Laboratory.
295 Briefly, 60 μL of sample (13–23 mg/mL *PcaLOOL* produced in *P. pastoris*) was injected onto a
296 Superdex 200 Increase 5/150GL column (Cytiva) using an Agilent 1260 Infinity II Bio Inert

297 HPLC system (Agilent Technologies, CA, USA). The flow rate was set to 0.35 mL/min and
298 eluate from the column was split 2:1 via a passive splitter between the X-ray flow cell and UV
299 branch, respectively (48). SAXS/WAXS images of 2 s exposures and 350 frames were collected
300 simultaneously on a Pilatus 1M (SAXS) and Pilatus 900K (WAXS) detector. Data from both
301 detectors were merged, scaled, and normalized to the water peak scattering intensity using LiX
302 beamline software, py4xs and lixtools, as described elsewhere (49,50).

303

304 **SAXS analysis of protein samples.** BioXTAS RAW program and ATSAS suite were used for
305 analysis of the SAXS data (51,52). The pair distance distribution function ($P(r)$), implemented in
306 RAW, was calculated using the indirect Fourier transform method using GNOM (53). The
307 SAXS-derived molecular weight was determined using the volume of Porod method in RAW
308 (54). The experimental SAXS data were compared to theoretical scattering curves generated
309 from atomistic models using the FOX program (55,56). Protein conformational sampling was
310 performed using AlphaFold2 (57) and Normal Mode Analysis (ATSAS). Chimera was used to
311 visualize PDB structures (58).

312

313 **Treatment of native wood and holocellulose samples with *Pca*LOOLs.** Acetone extracted
314 native wood and holocellulose samples (2 mm x 1 mm x 20 mm) were soaked in a freshly
315 prepared sodium acetate buffer (20 mM, pH 5.5, in 100 % D₂O) followed by three solvent
316 exchanges over 24 h to ensure the maximum number of accessible exchangeable hydrogen atoms
317 were exchanged with deuterium atoms in the samples. After deuterium exchange, 1.4 mg of
318 *Pca*LOOL proteins produced in *P. pastoris* were separately mixed with 70 mg of wood sample
319 or holocellulose in a glass vial and the final volume adjusted to 4.0 mL with the sodium acetate

320 buffer. Control samples were prepared in the same manner but without the addition of protein.
321 The control and analytical samples were agitated at 400 rpm in a mechanical shaker at 40 °C for
322 24 h. Native, unextracted wood samples were also exchanged into D₂O buffer and incubated at
323 room temperature (~25 °C) with no shaking.

324

325 **SANS data collection.** Approximately 3-5 slices of each treated wood and holocellulose sample
326 were carefully placed side-by-side in titanium sample cells with each slice vertically aligned
327 perpendicular to the incident beam. The cells were filled with the deuterated sodium acetate
328 buffer solution. SANS measurements were performed at the Bio-SANS (CG-3) instrument
329 located at the High Flux Isotope Reactor (HFIR) in the Oak Ridge National Laboratory (ORNL).
330 The main detector array was at 15.5 m from the sample, and the curved wing detector array at
331 1.13 m from the sample and rotated 1.4° from the direct beam. Using this detector configuration,
332 the Q ranges obtained using 6 Å neutrons were $0.003 < Q \text{ (Å}^{-1}\text{)} < 0.8$, and the spread in
333 wavelength ($\Delta\lambda/\lambda$) was 13.2%.

334

335 The vertical arrangement of the sliced wood stems maintained the inherent alignment of the plant
336 cell wall structure, mainly cellulose microfibrils aligned along the stem growth direction. These
337 samples produce an anisotropic 2D scattering pattern. The raw 2D images were processed by
338 correcting for detector dark current, pixel sensitivity, normalizing to the incident beam monitor
339 counts, and subtracting scattering contribution from quartz cell and deuterated buffer. Two
340 scattering intensity profiles, I(Q) versus Q, were obtained from the equatorial (wedge 0) and
341 meridional (wedge 1) sectors of the 2D image. From the different scattering contributions in the
342 two sectors, the dominant scattering feature of the equatorial sector is the cellulose microfibril

343 structure while in the meridional sector it is the isotropic matrix copolymer. To isolate the
 344 cellulose microfibril feature, the meridional scattering contribution was then subtracted from the
 345 equatorial sector and analyzed as detailed below. More information about wedge reduction can
 346 be found in a prior publication (59).

347

348 **SANS data analysis.** The SANS data were analyzed using the Modeling II tool implemented in
 349 the Irena package (60) in Igor Pro 8.0 software (WaveMetrics, OR, USA). The basic small-angle
 350 scattering formula for scattered intensity $I(Q)$ is

$$351 \quad I(Q) = |\Delta\rho|^2 S(Q) \int_0^\infty |F(Q, r)|^2 V(r)^2 NP(r) dr \quad (1)$$

352 where $\Delta\rho$ is the contrast between scattering particle and solvent $|\rho_{particle} - \rho_{solvent}|$, $F(Q, r)$ is
 353 the scattering form factor of the cylindrical particles, $V(r)$ is the particle volume of size r , N is
 354 the total number of scattering particles, $P(r)$ is the Gaussian probability density distribution of
 355 the scattering particles of size r , and $S(Q)$ is the structure factor modeled with a hard sphere
 356 structure factor unless there is no need then $S(Q) = 1.0$. The equatorial SANS profiles of
 357 Eucalyptus and Spruce were modeled using a cylindrical form factor in the high Q region ($Q \sim$
 358 $0.05 - 0.4 \text{ \AA}^{-1}$) for all samples to represent the cellulose microfibril. The mathematical
 359 formulation of the cylindrical form factor is given by,

$$360 \quad P(Q) = \frac{scale}{V_{cyl}} \int_0^\pi f^2(Q, \alpha) \sin\alpha d\alpha \quad (2)$$

$$361 \quad f(Q, \alpha) = 2(\rho_{cyl} - \rho_{solv}) V_{cyl} j_0(Q \times H \cos\alpha) \frac{J_1(Q \times r \sin\alpha)}{(Q \times r \sin\alpha)} \quad (3)$$

$$362 \quad S(Q) = \frac{1}{1 + k \times \frac{3 \times (\sin(Q\zeta) - Q\zeta \times \cos(Q\zeta))}{(Q\zeta)^3}} \quad (4)$$

363

364 where H is half the cylinder length ($L=2H$), r is the cross-sectional radius of the cylinder, α is
365 the orientation angle of the cylinder's long axis, and J_1 is a first-order Bessel function. The low
366 Q data ($Q \sim 0.003 - 0.05 \text{ \AA}^{-1}$) was fit to a power-law function (using the Unified Fit function),
367 given by $I(Q) = B * Q^{-\alpha}$, where α is the power-law slope of the scattering curves, and B is the
368 scale factors of the power-law function (61). For subtracted equatorial 1D SANS profiles of
369 samples and controls, a structure factor was also included in the fitting. The convergence of the
370 fit using Genetic optimization was based on minimizing the chi-squared (χ^2) value of the fit for
371 the entire data range. The structure factor that accounts for the weak correlation is given in
372 equation 4 and is used to model the correlation between cellulose microfibrils. Here, k describes
373 the degree of correlation ($0 < k < 5.92$), and ζ is the average center-to-center distance between
374 microfibrils (62).

375

376 The meridional SANS data of Eucalyptus and Spruce were modelled by using a three-level fit.
377 The high Q ($Q \sim 0.075 - 0.4 \text{ \AA}^{-1}$) region was modelled by the spherical form factor given as,

$$378 \quad P(q) = \frac{\phi}{V_{sph}} \frac{3[\sin(QR_{sph}) - QR_{sph}\cos(QR_{sph})]^2}{(QR_{sph})^3} \quad (5)$$

379 where, F is the volume fraction of spheres and $V_{sph} = \frac{4}{3}\pi R_{sph}^3$ is the volume of a sphere of
380 radius R_{sph} . In addition, two slopes of different Q -exponents were observed in the intermediate Q
381 region ($Q \sim 0.01 - 0.075 \text{ \AA}^{-1}$) and low Q region ($Q \sim 0.003 - 0.01 \text{ \AA}^{-1}$), and these two regions
382 were fit using two power-law functions (by using two levels of the Unified Fit function)
383 described above (60).

384

385 RESULTS AND DISCUSSION

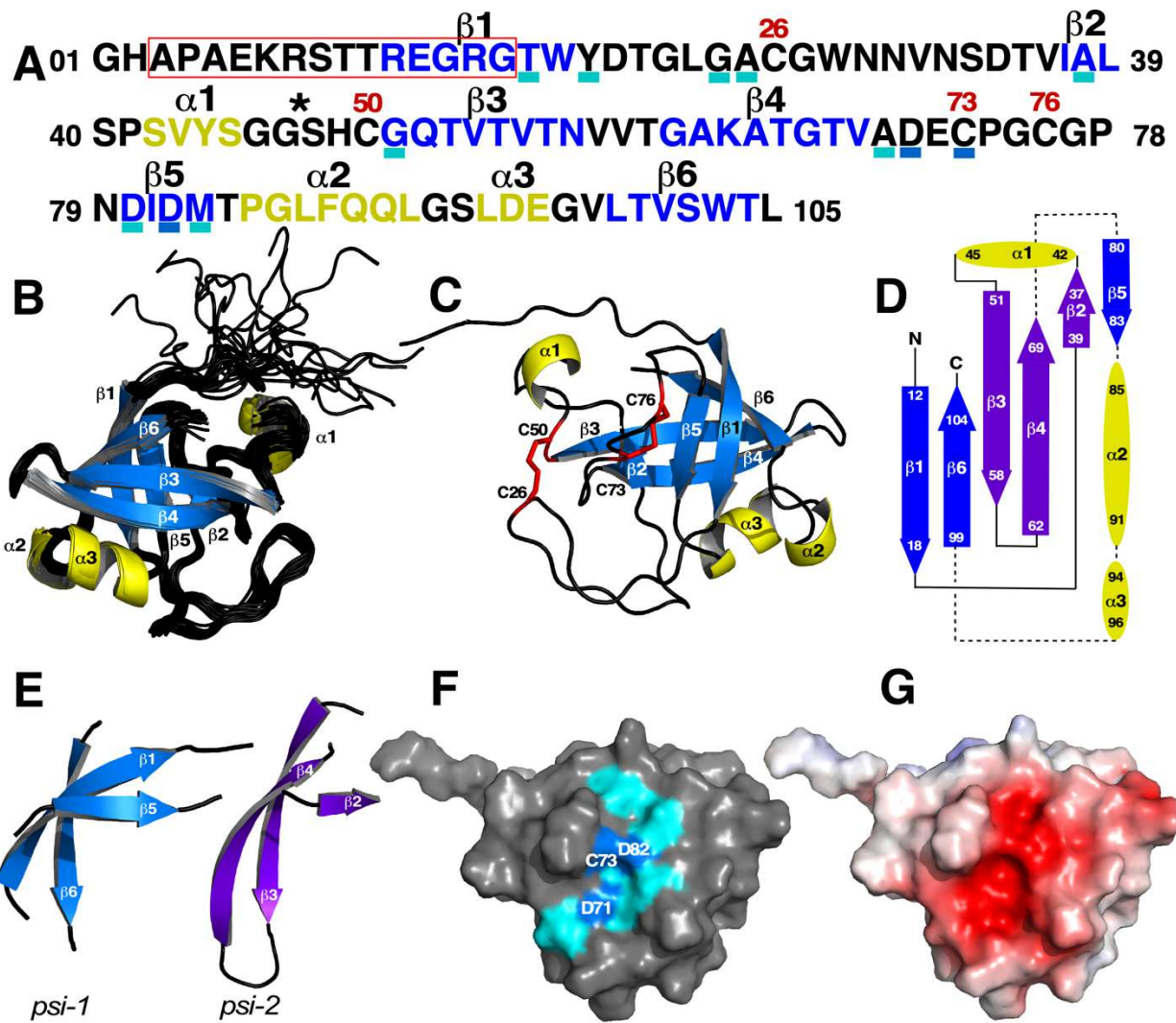
386 Three loosenins from *P. carnosus* (*PcaLOOL7*, *PcaLOOL9*, and *PcaLOOL12*) were
387 characterized in terms of their solution structures and impacts on lignocellulosic materials. For
388 these studies, *PcaLOOL7*, *PcaLOOL9* and *PcaLOOL12* were recombinantly produced in *P.*
389 *pastoris*, achieving yields of 174, 479, and 303 mg/L, respectively (Figure S1). SANS was then
390 used to compare the structural effects of these loosenins on holocellulose substrates prepared
391 from softwood (Spruce, *Picea abies*) and hardwood (Eucalyptus, *Eucalyptus grandis*) chips that
392 comprise varying lignin and hemicellulose contents.

393
394 **Structural characterization of the *PcaLOOLs* used for holocellulose treatment.** Besides
395 recombinant production in *P. pastoris*, it was possible to obtain milligram amounts of soluble
396 *PcaLOOL12* in *E. coli* by fusing thioredoxin to the N-terminal of the protein. *PcaLOOL12*
397 produced in *E. coli* remained soluble following thioredoxin cleavage and removal, enabling the
398 ¹³C- and ¹⁵N-labeling of *PcaLOOL12* and calculation of an NMR solution structure. The
399 assigned ¹H-¹⁵N HSQC spectrum for *PcaLOOL12*, illustrated in Figure S2, features sharp and
400 uniform cross peaks with wide chemical shift dispersions in both dimensions, general
401 characteristics of a small, folded protein (63). The estimated rotational correlation time for
402 *PcaLOOL12*, calculated from a series of 1-D, ¹⁵N-edited proton spectra, was 4.7 ± 1.1 ns, a
403 value expected for a 10.8 kDa protein (64). These features, along with a late elution time on a
404 Superdex75 size exclusion column (data not shown), indicated that *PcaLOOL12* was a monomer
405 in solution.

406
407 As illustrated in Figure S2 and tabulated in the chemical shift assignments deposited into the
408 BMRB, 96 out of the expected 99 backbone amide resonance cross peaks ($105 - (\text{N-terminal} + 5$

409 prolines)) were assigned in the ^1H - ^{15}N HSQC spectrum of *Pca*LOOL12. This enabled nearly
410 complete assignment of all the backbone and side chain protons critical for the auto-assignment
411 of the peak-picked NOE data. Consequently, as summarized in Table S2, 1300 NOE based
412 distance restraints (of which nearly 500 were long range), 68 hydrogen bond restraints, a total of
413 150 Phi and Psi torsion angle restraints, and 6 disulfide bond restraints were used in the final set
414 of structure calculations. This resulted in good convergence of the final ensemble of 20
415 structures as shown in the cartoon ensemble, superimposed over the ordered regions, in Figure
416 1B. The RMSD of the structured core from the mean structure was 0.50 ± 0.07 Å for the
417 backbone atoms (N-C $^\alpha$ -C=O) and 0.84 ± 0.06 Å for all heavy atoms (Table S2). The good
418 quality of the final set of structures is further corroborated by an analysis of these structures with
419 the PSVS validation software package (47) as tabulated in Table S2. Ramachandran statistics for
420 the Phi/Psi pairs were all in favored (90.7 %) or additionally allowed (9.3 %) regions with the
421 structure-quality Z-scores all above acceptable levels (>-4).

422



423

424 **Figure 1.** Solution NMR structure of *Pca*LOOL12 (9CE9). (A) The primary amino acid
 425 sequence of *Pca*LOOL12 with the β -strand and α -helix elements of secondary structure colored
 426 blue and yellow, respectively. Disulfide bonds are observed between C26-C50 and C73-C76
 427 with the position of these four cysteine residues identified with red residue numbers above the
 428 sequence. The *P. carnos*a genome contains 12 loosenin genes divided into two subgroups based
 429 on the position of an insertion relative to the predicted polysaccharide binding groove
 430 (*Pca*LOOL12 belongs in subgroup B) (15). The red box is the characteristic 12-18 residue
 431 insertion observed in subgroup B loosenins and the asterisk after G44 indicates the position of
 432 the characteristic 8-9 residue insertion observed in subgroup A loosenins. The rectangles below
 433 the sequence denote conserved residues in the *P. carnos*a loosenin family predicted to form a
 434 polysaccharide binding groove, with the blue rectangles denoting residues associated with

435 expansin activity (EXLX1) in this groove. The first two N-terminal residues are “scars” left over
436 after cleavage of the thioredoxin moiety of the original construct. The six β -strands form a
437 double-*psi* β -barrel (DPBB) structural fold. (B). A cartoon superposition of the ensemble of 20
438 solution structures calculated for *Pca*LOOL12. (C) A cartoon representation of a single structure
439 in the ensemble rotated 180 ° in the y-axis to better illustrate the location of the two disulfide
440 bonds (side chains colored red) and the three β -strands on the back side of the protein. (D) A
441 topology diagram illustrating the relative orientation of the elements of secondary structure with
442 the α -helices colored yellow and the β -strands colored blue (*psi-1*) or purple (*psi-2*). The β -
443 strands and α -helices are drawn to scale but not the connecting loops and turns. (E) Isolation of
444 the two *psi* motifs in the DPBB structural fold. (F) A view similar to (C) of the solvent-
445 accessible surface of *Pca*LOOL12 with the residues predicted to form a polysaccharide binding
446 groove colored cyan or blue (A). The three labeled blue residues are associated with activity in
447 expansins. (G) A view identical to (F) highlighting the electrostatic potentials at the solvent-
448 accessible surface of *Pca*LOOL12 (-5 to +5 kT/e) with the negative and positive regions colored
449 red and blue, respectively.

450

451

452 The elements of secondary structure observed in the solution structure of *Pca*LOOL12 are
453 summarized in its primary amino acid sequence in Figure 1A and labeled on the tertiary structure
454 of the protein in the ensemble in Figure 1B and the single structure closest to the average in
455 Figure 1C (rotated 180 ° in the y-axis relative to the ensemble). Figure 1D is a topology diagram
456 to assist visualization of the organization of the elements of secondary structure, six β -strands
457 and three α -helices, in the tertiary structure. The six β -strands hydrogen bond in a continuous
458 fashion to form a barrel-like structure composed of two similar, three-strand units distinguished
459 in blue and purple in the topology diagram. As illustrated in Figure 1E, three β -strands form a
460 *psi*-motif composed of two relatively long antiparallel β -strands with the C-terminal of the C-
461 terminal strand bent significantly relative to the N-terminal of the N-terminal strand, with a short

462 strand running parallel to the C-terminal of the C-terminal strand (65). As illustrated best in
463 Figure 1D, the two *psi*-motifs (*psi*-1: β 6- β 1- β 5 ($\downarrow\uparrow\uparrow$); *psi*-2: β 3- β 4- β 2 ($\downarrow\uparrow\uparrow$)) are
464 positioned relative to each other to allow the short strands, β 5 and β 2, to form an anti-parallel
465 pair to interlock the *psi*-motifs with an overall pseudo-twofold axis between the motifs. Such a
466 fold is called a double- ψ β -barrel (DPBB) and has been observed in a number of unrelated
467 proteins including aspartate- α -decarboxylase, dimethyl sulfoxide reductase, barwin,
468 endoglucanase V, and an endo-chitosanase (65, 66). Around the core DPBB fold are three α -
469 helices, with the largest one, α 2, nestled against the core and the two smaller ones part of loops
470 extending from the core. Note that the largest loop, between β 1 and β 2, is tethered to the DPBB
471 core fold at the N-terminal of β -3 via a disulfide bond, C26-C50 (Figure 1C, red). A second
472 disulfide bond, C73-C76, is present in the loop between β 4 and β 5 with C73 forming part of the
473 predicted polysaccharide binding groove (Figure 1F). Figure 1F also shows that most of the
474 residues predicted to form a surface accessible polysaccharide binding groove (cyan and blue
475 underlined residues in Figure 1A) are surface exposed in the three-dimensional structure of
476 *Pca*LOOL12 (residues A70 and M83 are buried in the middle of the protein and G50 is on the
477 opposite face). Figure 1G shows that the surface of this face of the protein is negatively charged.
478 A search for structures similar to *Pca*LOOL12 using the Dali server (67) identified seven
479 structures with a Z-score greater than 8.5, six of these with a Z-score greater than 10 (Figure S3).
480 In addition to expansin-related proteins, the structures include a protein annotated as a papain
481 inhibitor from *Streptomyces mobaraensis* (5NTB) (68), hypothetical protein Pa4485 from
482 *Pseudomonas aeruginosa* (4AVR) (72), kiwellin (4X9U) (69), the most abundant protein found
483 in gold kiwifruit (*Actinidia chinensis*) (70), and an auxiliary metabolic gene (AMG) product (V-

484 Csn; 7TVL) displaying endo-chitinase activity from a soil phage identified in a metagenomic
485 survey (71).

486

487 Previously, the 12 loosenins in the *P. carnosus* genome were divided into two subgroups, A and
488 B, based on the position of an insertion relative to the predicted polysaccharide binding groove
489 (15). *Pca*LOOL12 belongs in subgroup B due to a 14-residue insertion outlined in the red box in
490 Figure 1A. On the other hand, *P. carnosus* loosenin classified into subgroup A have an 8-9
491 residue insertion at the position marked with an asterisk (Figure 1A). It was hypothesized that
492 these insertions might confer different polysaccharide binding specificity for these two
493 subgroups of loosenins (15). In the subgroup B *Pca*LOOL12 structure presented here, the C-
494 terminal five residues of the insertion are part of a β -strand in the DPBB fold with the rest of the
495 residues unstructured on the opposite face of the predicted polysaccharide binding groove
496 (Figure 1F). Although it is difficult to imagine this region directly influencing the polysaccharide
497 binding groove, the absence of the subgroup B insertion could impact the relative performance of
498 loosenins in yet to be discovered ways. The location of the insertion in subgroup A loosenins is
499 between β -strands β 2 and β 3, C-terminal to α 1 in Figure 1C. Such an insertion may be able to
500 fold into the predicted polysaccharide binding groove or extend the groove's breadth to effect
501 polysaccharide binding specificity. An experimental structure of at least one *P. carnosus*
502 subgroup A loosenin is necessary to distinguish these possibilities.

503

504 Temperature dependent NMR and circular dichroism (CD) experiments on *Pca*LOOL12 showed
505 the protein to be stable to high temperatures. Figure S4 shows a series of ^1H - ^{15}N HSQC spectra
506 collected on the same 0.2 mM sample of ^{15}N -labeled *Pca*LOOL12 at 20 °C, 60 °C, and back at

507 20 °C. While the spectrum at 60 °C contains only a few poorly dispersed amide cross peaks
508 suggestive of an unfolded protein, after cooling the sample back to 20 °C the ¹H-¹⁵N HSQC
509 spectrum is very similar to the spectrum collected prior to heating (there is evidence of some new
510 resonances appearing above the noise suggesting the refolding is not 100% efficient). Similar CD
511 experiments performed on a 0.02 mM sample of *PcaLOOL12* from 10 to 80 °C also suggested
512 *PcaLOOL12* unfolded at high temperature and refolded after heating (data not shown). Note
513 further that there was no visible evidence of protein precipitation after heating either in a CD cell
514 or NMR tube. Thermal stability ($T_m = 85$ °C) was also reported for the papain inhibitor from *S.*
515 *mobaraensis* (5NTB) that is structurally similar to *PcaLOOL12* (Figure S2) (68,72). Both
516 proteins contain two disulfide bonds in the same relative positions and disulfide bonds are known
517 to increase the stability of proteins and peptides (73). While additional experiments will be
518 necessary to confirm if these disulfide bonds are responsible for the observed thermal stability,
519 they are likely not required to stabilize the tertiary structure of *PcaLOOL12* as its structure is
520 very similar to the structure of *P. aeruginosa* Pa4485 (4AVR, Figure S3) despite the absence of
521 any cysteine residues in the latter protein.

522

523 The structure of *PcaLOOL12* produced in *P. pastoris* was then evaluated by size-exclusion
524 chromatography coupled with small-angle X-ray scattering (SEC-SAXS). The SEC-SAXS
525 profile showed a single peak between SAXS frames 209 and 256, and the radius of gyration (R_g)
526 values calculated from the individual SAXS profiles showed a decrease from approximately 18
527 Å to 15 Å across the elution peak (Figure S5). Evolving Factorial Analysis (EFA) was used to
528 deconvolute the different species in the SEC-SAXS profile and identified *PcaLOOL12*
529 oligomers with calculated R_g values of 15.7 ± 0.2 Å and 23.2 ± 0.6 Å (Table 1). The smaller

530 component was consistent with the NMR structure of the *PcaLOOL12* produced in *E. coli*, a
531 monomer with a molecular weight (MW) of 12.6 kDa. The larger MW species is consistent with
532 a *PcaLOOL12* dimer (MW = 24.5 kDa). The slightly larger MW of the *PcaLOOL12* monomer
533 obtained by SEC-SAXS (12.6 kDa) compared to NMR (10.8 kDa) is due to the presence of the
534 C-terminal His₆-tag in the former. Despite this, the NMR conformers provided a reasonably good
535 fit to the SAXS data (χ^2 of 3.60 and 7.28 for the NMR conformer with the best and worst fit,
536 respectively). Notably, the AlphaFold2 *PcaLOOL12* structure is very similar to that of NMR
537 structure that best fit the SAXS data (χ^2 of 3.60). The backbone root-mean-square deviation
538 (RMSD) between the AlphaFold2 and NMR structures is 0.71 Å for residues 1 to 103, excluding
539 the C-terminal His₆-tag present in the AlphaFold2 model (Figure S6). Using the AlphaFold2
540 *PcaLOOL12* model that included the His₆-tag yielded a SAXS fit of $\chi^2 = 4.8$, indicating that the
541 addition of the His₆-tag alone does not account for the protein's structural flexibility observed in
542 SAXS (Figure 2). Normal Mode Analysis (NMA) was then used to calculate flexible motions
543 within the protein, which provided a conformation of *PcaLOOL12* with NMA χ^2 value of 1.5
544 (Figure 2). The RMSD for the backbone between the NMA and NMR models was 1.40 Å for
545 residues 1 to 103. Most of the significant differences in the amino acid backbone RMSD were
546 observed in the N-terminal region (residues 1 – 12) (Figure S7), which was also identified as a
547 highly flexible region in our NMR structure. This highly flexible N-terminal, combined with the
548 presence of the His₆-tag, provided good agreement between the NMA model and the SAXS data.
549

550 Although NMR structures were not determined for *PcaLOOL7* and *PcaLOOL9*, the agreement
551 between the SEC-SAXS derived model of *PcaLOOL12* and its NMR structure supports the
552 structural assessment of *PcaLOOL7* and *PcaLOOL9* using SEC-SAXS alone. The elution profile

553 of *PcaLOOL7* showed a single peak between SAXS frames from 180 to 220, and the R_g values
554 calculated from the individual SAXS profiles showed a decrease from 17.8 Å to 13.7 Å across
555 the elution profile (Figure S5). Using EFA to deconvolute the SEC-SAXS profile, two major
556 components were obtained with R_g values of 17.1 ± 0.1 Å and 13.4 ± 0.3 Å (Table 1). The larger
557 species is consistent with a *PcaLOOL7* monomer with a MW of 14.9 kDa; the smaller particle
558 had a MW of 11.1 kDa and was likely due to proteolytic degradation of the holoprotein. The
559 predicted AlphaFold2 model fit the SAXS data of *PcaLOOL7* reasonably well (χ^2 of 6.0)
560 (Figure S8) and improved using NMA (NMA χ^2 value of 1.6) (Figure 2).

561
562 A similar approach was used to analyze *PcaLOOL9*. In this case, the SEC-SAXS profile also
563 showed a single peak between SAXS frames 160 and 220 (Figure S5). The R_g values calculated
564 from the individual frames decreased from approximately 67 Å to 20 Å across the elution peak.
565 EFA also showed the presence of *PcaLOOL9* oligomers with MW values ranging between 320
566 kDa and 18.8 kDa, a considerably wider range than observed for *PcaLOOL12* and *PcaLOOL7*.
567 The R_g values of the SAXS frames plateau between frame 200 – 220 and the calculated MW and
568 R_g were 11.9 kDa and 15.7 ± 0.1 Å (Table 1), respectively, consistent with a *PcaLOOL9*
569 monomer. Unlike *PcaLOOL12* and *PcaLOOL9*, the predicted AlphaFold2 model did not
570 provide a good fit to the SAXS data of *PcaLOOL9* (χ^2 of 31.7) (Figure S8); however, NMA
571 provided conformations that fit the data for *PcaLOOL9* with a χ^2 value of 2.5 (Figure 2).
572 Notably, the structures generated from NMA for all three *PcaLOOL* proteins were similar to the
573 AlphaFold2 models except for the N-terminal region (1 – 26) and the unstructured C-terminus
574 His₆-tag, which were predicted with relatively low confidence (predicted local distance
575 difference test (pLDDT) between 50 – 70%).

576 **Table 1:** Structural parameters and data fitting of *PcaLOOL* proteins from SEC-SAXS

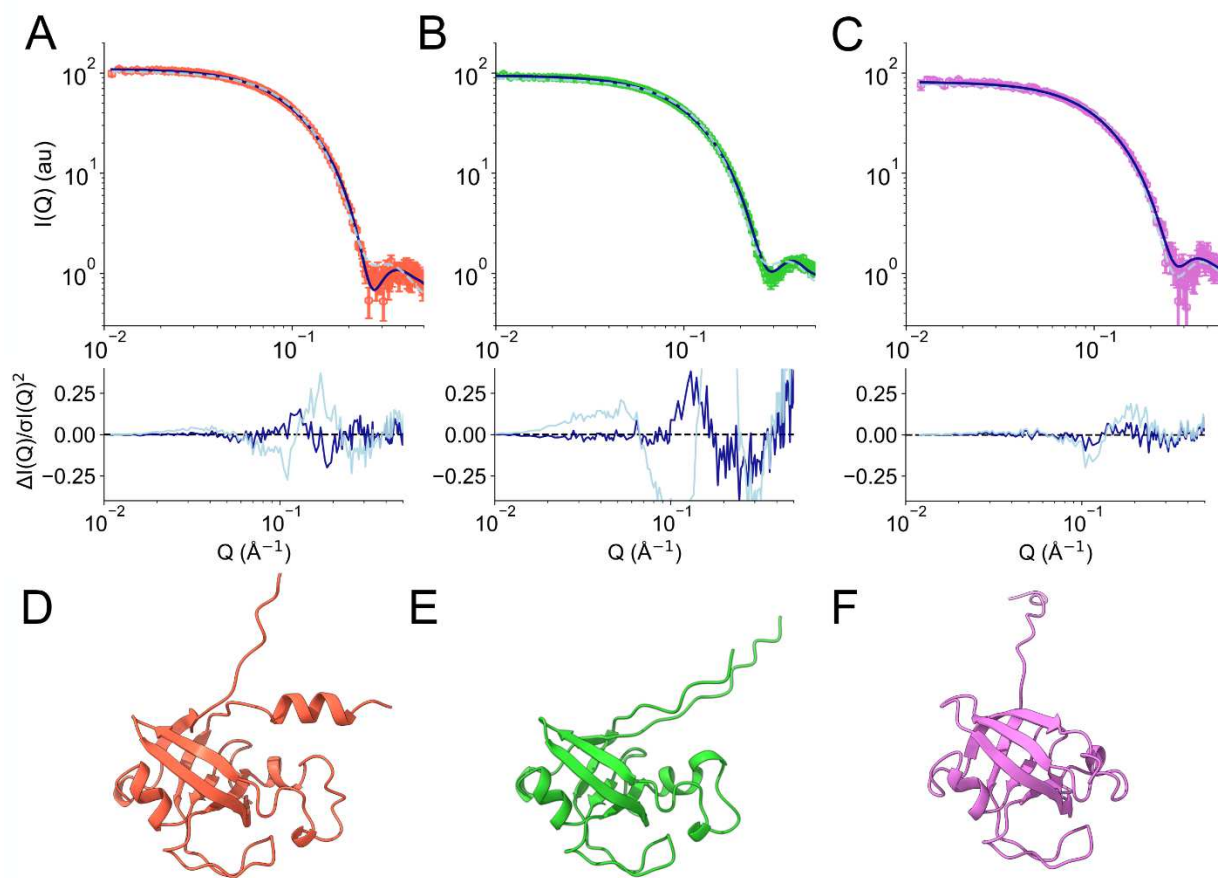
	<i>PcaLOOL7</i>	<i>PcaLOOL9</i>	<i>PcaLOOL12</i>
Guinier analysis			
$I(0)$ (a.u)	109.7± 0.3	93.5± 0.1	82.7± 0.4
R_g (Å)	17.1 ± 0.1	15.7 ± 0.1	15.7 ± 0.2 Å
$Q \times R_g$ range	0.23 - 1.29	0.30 – 1.30	0.20 - 1.28
$P(r)$ analysis			
$I(0)$ (a.u)	109.8 ± 0.3*	94.6 ± 0.2	83.8 ± 0.5
R_g (Å)	17.9 ± 0.2	16.4 ± 0.1	16.5 ± 0.3
D_{max} (Å)	72	91	60
Q range (Å ⁻¹)	0.14–0.5	0.013–0.4	0.012–0.3
χ^2	<1.0	1.0	1.2
Molecular weight (M_w) analysis			
M_w from Porod volume (kDa)	14.9	11.9	12.6

577 * $I(0)$ from SEC-SAXS is not on absolute scale; Theoretical molecular weights (calculated from
578 their primary amino acid sequences) of *PcaLOOL7*, *PcaLOOL9*, and *PcaLOOL12* are 13.44
579 kDa, 11.98 kDa, and 11.4 kDa, respectively.

580

581

582



583

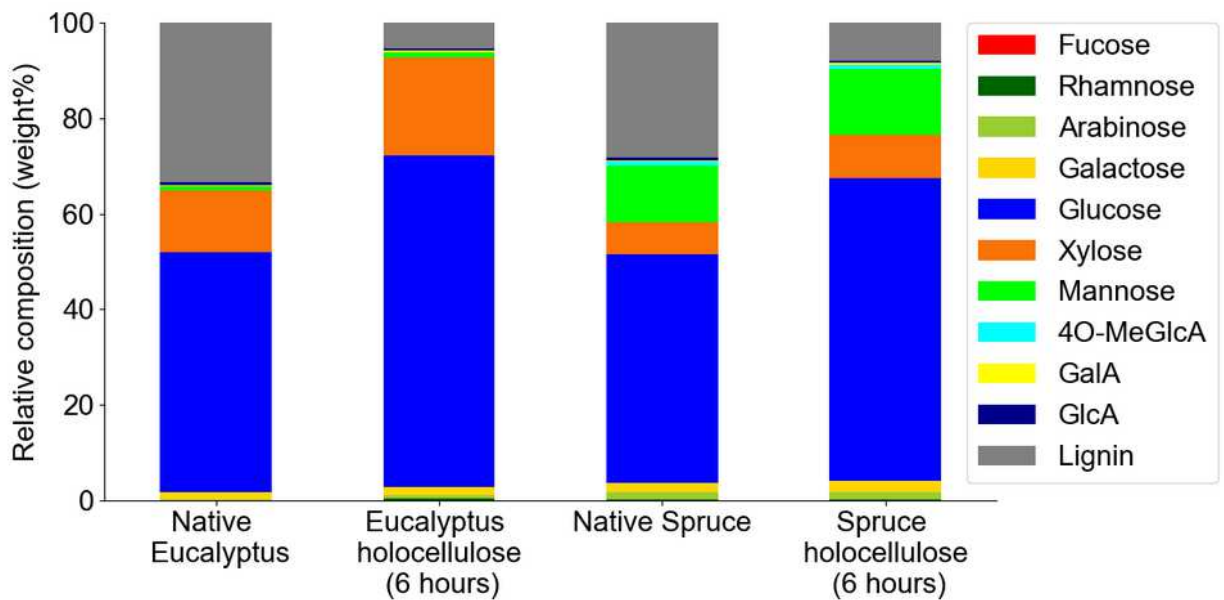
584 **Figure 2.** Structural analysis of *PcaLOOLs*. Panels A to C) Experimental SAXS profiles of
 585 *PcaLOOL7* (orange), *PcaLOOL9* (green), and *PcaLOOL12* (pink) are shown as open hexagons.
 586 Theoretical SAXS profiles from AlphaFold2 and Normal Mode Analysis are shown as dashed
 587 light and solid dark blue lines, respectively. Error-normalized residual plots are show below the
 588 SAXS profiles. Panels D to F) Normal Mode Analysis models of *PcaLOOL7* (orange),
 589 *PcaLOOL9* (green), and *PcaLOOL12* (pink).

590

591 **Characterization of native wood samples and holocelluloses prior to *PcaLOOL* treatment.**

592 Compositional analyses of native and delignified Eucalyptus and Spruce samples confirmed the
 593 efficacy of the sodium hypochlorite delignification treatment (Figure 3, Table S3). Specifically,
 594 after 6 h, the sodium hypochlorite treatment reduced the lignin content of Eucalyptus samples by
 595 87%, from 36 wt% to 5 wt% of the total sample. Similarly, the lignin content of Spruce samples

596 was reduced by 75%, from 28 wt% to 8 wt% of the total sample. In parallel, the monosaccharide
 597 composition revealed that the delignification process did not significantly alter the cellulose and
 598 hemicellulose populations in the Eucalyptus and Spruce wood samples. The Eucalyptus
 599 holocellulose fibers showed a cellulose content of approximately 57 wt%, retaining a
 600 hemicellulose content of 18 wt%, in which (galacto)glucuronoxylan was, as expected, the most
 601 dominant component with a negligible content of glucomannan (< 2 wt%). In parallel, the Spruce
 602 holocellulose fibers contain approximately 59 wt% of cellulose and retained a total hemicellulose
 603 content of approximately 29 wt%, where galactoglucomanan was the most abundant component
 604 (18 wt%) with a significant content of arabinoglucuronoxylan (11 wt%).
 605



606
 607 **Figure 3.** Relative monosaccharide and lignin composition of untreated wood (Eucalyptus and
 608 Spruce) and holocellulose samples. Values represent the relative weight of the corresponding
 609 monosaccharide from acid hydrolysis and the measured lignin after the acetyl bromide
 610 dissolution in the total weight of the biomass sample.
 611

612 The impact of partial delignification and varying hemicellulose contents on holocellulose
613 structure was investigated using SANS. Especially, equatorial scattering is of importance where
614 overall intensity in the equatorial region (low Q values) of the SANS data can point to cellulose
615 microfibrillar morphology and order aligned along the stem growth direction as well as the
616 morphology of nanopores within the wood cell wall in some cases (74, 75). By contrast, the
617 meridional (or vertical) scattering region is dominated by the amorphous components in the cell
618 wall such as residual lignin, hemicellulose, and cellulose microfibrils aligned parallel to the
619 direction of the neutron beam (59).

620
621 The 2D SANS scattering patterns of native Eucalyptus and Spruce (Eu_native, Sp_native) and
622 holocellulose (Eu_HC, Sp_HC) are shown in Figure 4A-D. The differences in the images can be
623 attributed to the changes in the organization of the aligned cellulose microfibrils in the cell walls.
624 Both native Eucalyptus and Spruce generated a similar 2D scattering pattern; a sharp streak-like
625 pattern in the equatorial direction of the main detector and a lobe-like feature extended into the
626 wing detector image. This indicates that the cellulose microfibrils were well-aligned along the
627 growth direction of the plants (59,76). In contrast, the 2D scattering patterns of the holocellulose
628 samples were less defined compared to the native samples; moreover, the lobe feature in the
629 wing detector was missing indicating that the cellulose microfibril ordering decreased after lignin
630 removal.

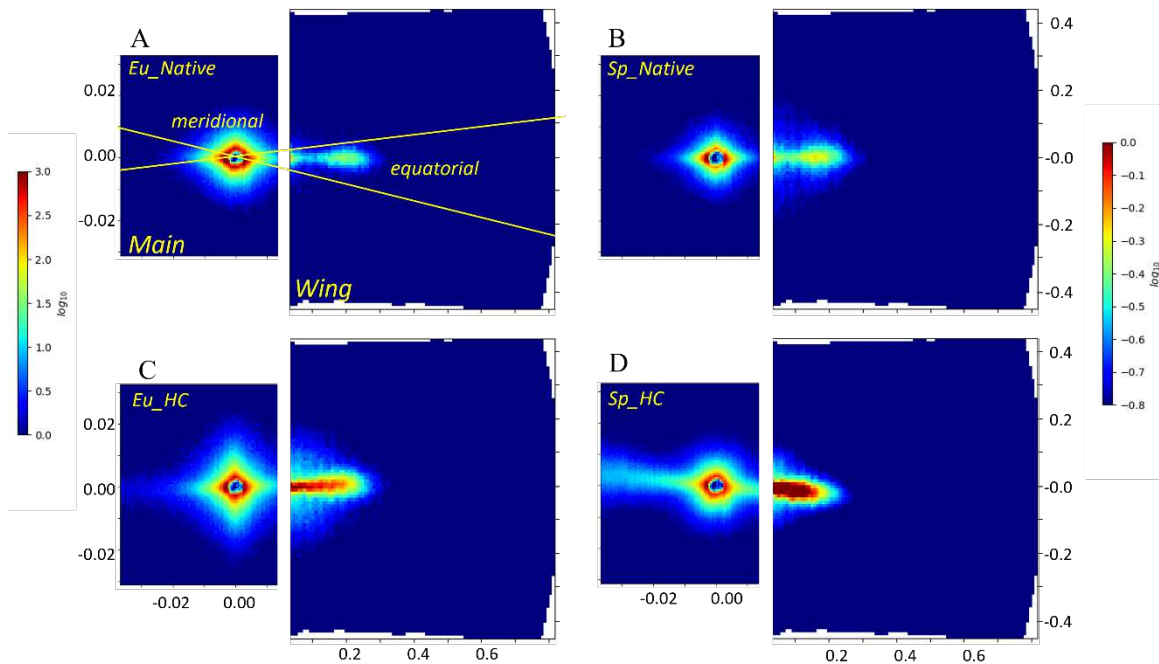


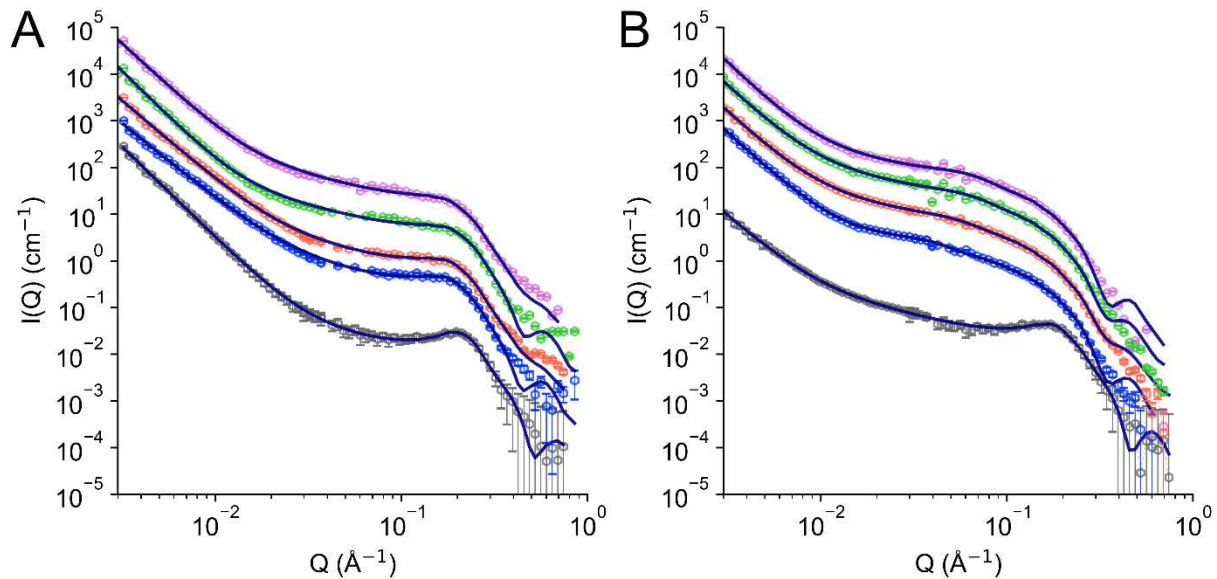
Figure 4. Two-dimensional SANS detector images of native Eucalyptus (A) and Spruce (B), and holocellulose from Eucalyptus (C) and Spruce (D) in 20 mM sodium acetate buffer, pH 5.5 in 100% D₂O. Each panel shows the main (left) and wing (right) detector images from the SANS instrument. Lines in the panel A represent the equatorial and meridional sectors that were used for data analysis and interpretation.

632

633 The 2D scattering patterns were reduced to 1D scattering profiles using the wedge reduction
 634 approach as described in the Materials and Methods to obtain equatorial and meridional curves
 635 of the native samples (grey profiles in Figure 5 and Figure 6, respectively). The equatorial
 636 profiles showed a well-defined peak in the high Q region ($Q \sim 0.05 - 0.4 \text{ \AA}^{-1}$) and specifically at
 637 $Q \sim 0.2 \text{ \AA}^{-1}$ that is attributed to the radial spacing between cellulose microfibrils aligned along
 638 the growth direction of the plants. In the low Q region ($Q \sim 0.003 - 0.05 \text{ \AA}^{-1}$), both native species
 639 exhibit a steep monotonic increase in intensity for decreasing Q values, which is attributed to the

640 existence of large structures (d of 0.1 – 0.2 μm) such as cellulose microfibrils or cell wall lumen
641 (Figure 5).

642



643

644 **Figure 5.** One-dimensional equatorial SANS profiles of Eucalyptus (A) and Spruce (B). The
645 color labeling schemes for the left and right panels are identical. The holocellulose samples were
646 incubated for 24 h with the *Pca*LOOL proteins before SANS measurements. Native wood
647 sample (grey); holocellulose control (blue); *Pca*LOOL7 (orange); *Pca*LOOL9 (green),
648 *Pca*LOOL12 (pink). The *Pca*LOOL7, *Pca*LOOL9, and *Pca*LOOL12 curves were multiplied by
649 multiples of 4, and native wood sample was multiplied by a factor of 0.16 for data visualization
650 purposes.

651

652 Quantitative analysis of the equatorial SANS profiles was performed using a model that
653 comprises of a cylindrical form factor coupled with a structure factor to model the high Q
654 signature ($Q \sim 0.05 - 0.4 \text{ \AA}^{-1}$), and a power-law for the low Q region ($Q \sim 0.003 - 0.05 \text{ \AA}^{-1}$). The
655 fitting parameters are listed in Table 2. The cross-sectional radius of the cylindrical particles,
656 representing cellulose microfibrils of native Eucalyptus and Spruce samples are $7.9 \pm 0.7 \text{ \AA}$ and
657 $8.3 \pm 0.7 \text{ \AA}$, respectively, which agrees well with previously reported values (29). The peak

658 feature in the high-Q region ($0.05 - 0.4 \text{ \AA}^{-1}$) provides a measure of the center-to-center distance
659 of neighboring cellulose microfibrils ($d_{spacing}$). The $d_{spacing}$ value of $30 \pm 3 \text{ \AA}$ for Spruce is
660 consistent with those previously reported for Sitka spruce (3-4 nm depending on moisture
661 content) (77). The $d_{spacing}$ value of $26 \pm 1 \text{ \AA}$ for Eucalyptus, however, was somewhat lower than
662 reported values for other angiosperms including birch (3.4 nm) and aspen (4 nm) (78, 79). The
663 generally higher microfibril spacing in angiosperms over gymnosperms has been attributed to the
664 higher xylan content in angiosperms and regular binding of the xylan to hydrophilic faces of
665 microfibrils (80–82), which could putatively accommodate a monolayer of xylan chains bound to
666 the cellulose surfaces in a similar 2-fold screw conformation. Although we cannot rule out
667 impacts of sample age and storage conditions of the Spruce and Eucalyptus wood chips used
668 herein, the comparatively low microfibril spacing (i.e., $d_{spacing}$ value) measured for Eucalyptus
669 could reflect the structure of Eucalyptus xylan, in which the presence of galactose substitutions
670 covalently bound to 4-*O*-methyl glucuronic acid decorations (82) might hinder xylan interactions
671 with cellulose surfaces.

672

673 The equatorial SANS profiles do not provide a scattering signature for macrofibrils because the
674 same water and amorphous polymer (lignin and hemicellulose) contrast exists between
675 individual microfibrils and the bundles that comprise the macrofibrils. Moreover, the loosely
676 defined boundary for macrofibrils potentially contribute to a larger polydispersity in the cross-
677 sectional radius of the macrofibrils making it difficult to observe. Nevertheless, the packing
678 parameter (k) estimates the degree of packing of cellulose microfibrils in the wood samples (64).
679 The most efficient packing arrangement, such as a hexagonally packed lattice or face-centered
680 cubic lattice, has a k value of 5.92 that decreases to zero in a random distribution of particles

681 (62). The packing parameter is 4.6 ± 0.2 and 3.6 ± 0.2 for Eucalyptus and Spruce, respectively
682 indicating that the cellulose microfibrils have a regular arrangement in both native samples
683 (Table 2).

684
685 The equatorial scattering profiles of the Eucalyptus and Spruce holocellulose were significantly
686 different from the native sample (Figure 5). The most visible change was the loss of the strong
687 peak feature in the high-Q region which represents the loss of regular order in the arrangement of
688 the cellulose microfibrils. This is consistent with the observed loss of a strong lobe-like feature in
689 the 2D patterns upon delignification. The cross-sectional radius of the cellulose microfibril did
690 not show appreciable change on delignification for either Eucalyptus or Spruce, consistent with
691 the potential lignin localization in the outer parts of microfibrils (83). In contrast, the values for
692 the $d_{spacing}$ in the Eucalyptus samples increased by 15 % from 26 Å to 30 Å; the increase was
693 more significant in Spruce where the $d_{spacing}$ values increased by 190 %, from 30 Å to 87 Å
694 (Table 2). The increase in center-to-center distance between neighboring cellulose microfibrils
695 was coupled with a decrease in the degree of order (i.e., packing parameter, f_{pack}), where f_{pack}
696 reduced from 4.6 to 2.8 in Eucalyptus and from 3.6 to 0.7 in Spruce (Table 2). The more
697 significant impacts of delignification on the regular arrangement of the cellulose microfibrils in
698 Spruce compared to Eucalyptus could be caused by a reorganisation of the corresponding
699 hemicelluloses (i.e., mainly the accessible acetylated galactoglucomannan populations in Spruce)
700 (84). This aligns well with the observation that softwood microfibrils may be more sensitive to
701 drying than hardwood microfibrils (85), indicating that the former could be more accessible and
702 thus more affected by delignification treatments, and potentially, the activity of loosening.

703

704 **Table 2.** Fitting parameters extracted from the equatorial SANS data analysis.

Sample	Cylinder				Power-Law Exponent
	Volume Fraction	R_{cs} (Å)	$d_{spacing}$ (Å)	f_{pack}	P
Q range (Å ⁻¹)	0.05-0.4				0.003- 0.04
Eu_native	0.051 ± 0.007	7.9 ± 0.7	26 ± 1	4.6 ± 0.2	3.8 ± 0.2
Eu_HC	0.094 ± 0.001	8.7 ± 0.9	30 ± 1	2.8 ± 0.3	3.6 ± 0.2
Eu_PcaLOOL12	0.079 ± 0.002	8.6 ± 1.5	29 ± 2	1.8 ± 0.2	3.7 ± 0.1
Eu_PcaLOOL7	0.060 ± 0.001	8.7 ± 1.6	29 ± 1	2.6 ± 0.3	3.6 ± 0.2
Eu_PcaLOOL9	0.078 ± 0.001	8.4 ± 0.7	29 ± 1	2.2 ± 0.2	3.9 ± 0.1
Sp_native	0.055 ± 0.001	8.3 ± 0.7	30 ± 3	3.6 ± 0.2	3.5 ± 0.1
Sp_HC	0.039 ± 0.002	10.9 ± 1.4	87 ± 6	0.7 ± 0.1	3.8 ± 0.1
Sp_PcaLOOL12	0.051 ± 0.001	10.9 ± 1.4	138 ± 10	0.7 ± 0.1	3.7 ± 0.1
Sp_PcaLOOL7	0.055 ± 0.001	10.9 ± 2.1	103 ± 8	0.5 ± 0.2	3.7 ± 0.2
Sp_PcaLOOL9	0.054 ± 0.001	11.1 ± 1.7	88 ± 4	0.6 ± 0.1	3.7 ± 0.1

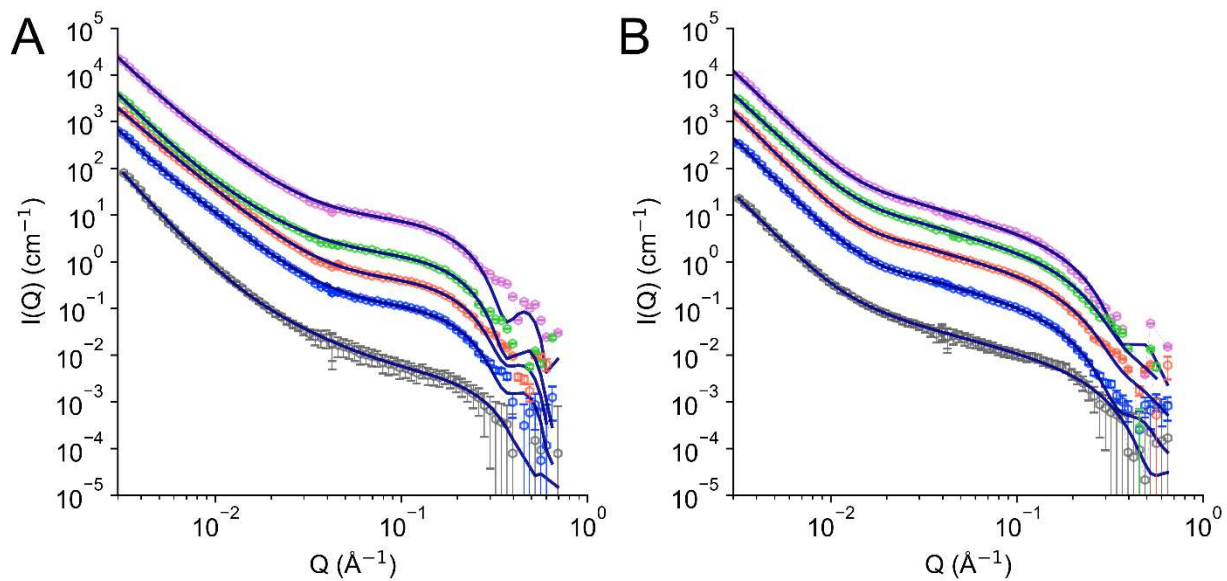
705 Eu: Eucalyptus; Sp: Spruce; HC: holocellulose

706

707 The SANS data in the meridional sector of the 2D pattern arise from the isotropic scattering
708 features in the plant cell wall such as the cellulose microfibrils aligned parallel or close to
709 parallel to the neutron beam direction, and the amorphous matrix of lignin and hemicellulose co-
710 polymers. The high Q region ($Q \sim 0.075 - 0.4 \text{ \AA}^{-1}$) was modelled to a spherical form factor and a
711 power-law function in the intermediate Q region ($Q \sim 0.01 - 0.075 \text{ \AA}^{-1}$) (Figure 6). The spherical
712 form factor represents the isotropic scattering feature of the cellulose microfibril aligned parallel
713 to the neutron beam. The cross-sectional radius of the cellulose microfibril assemblies were
714 similar for the native species, $9.3 \pm 2.2 \text{ \AA}$ for Eucalyptus and $11.9 \pm 1.0 \text{ \AA}$ for Spruce; however,

715 the power-law exponent that represent structural organization in the length scale of 8-60 nm were
716 different (Table 3). An exponent of approximately -2 (-2.1 ± 0.1) for the Eucalyptus samples
717 indicates a randomly flexible conformation of the matrix co-polymers implying more
718 overlapping and criss-crossing conformations, while an exponent of -1.4 (-1 to -2) for Spruce
719 samples indicates a matrix co-polymer conformation having limited flexibility and less
720 overlapping (86). SANS data in the low Q region ($Q \sim 0.003 - 0.01 \text{ \AA}^{-1}$) was similar in both
721 samples, exhibiting a power-law exponent of approximately -4 which suggests the presence of
722 micron-sized assemblies.

723



724

725 **Figure 6.** One-dimensional meridional SANS profiles of Eucalyptus (A) and Spruce (B). The
726 color labeling schemes for the left and right panels are identical. The holocellulose samples were
727 incubated for 24 h with the *PcaLOOL* proteins before SANS measurements. Native wood
728 sample (grey); holocellulose control (blue); *PcaLOOL7* (orange); *PcaLOOL9* (green), and
729 *PcaLOOL12* (pink). The *PcaLOOL7*, *PcaLOOL9*, and *PcaLOOL12* curves were multiplied by
730 multiples of 4, and native wood sample was multiplied by a factor of 0.16 for data visualization
731 purposes.

732

733 Delignification led to an increase in the cellulose microfibril cross-sectional radius from $9.3 \pm$
734 2.2 \AA to $12.4 \pm 0.2 \text{ \AA}$ for Eucalyptus and from $11.9 \pm 1.0 \text{ \AA}$ to $19.7 \pm 1.0 \text{ \AA}$ for Spruce (Table 3,
735 Figure 6). The higher extent of increase in the cross-sectional radius for Spruce than for
736 Eucalyptus indicates a higher degree of misaligned cellulose microfibrils from the parallel
737 alignment to the neutron beam. This is consistent with the higher degree of loss of order for
738 Spruce as also measured from the equatorial sector, again suggesting greater impact of
739 delignification on the mobility of the remaining hemicellulose. At the same time, the matrix co-
740 polymer conformation remained unchanged between native and delignified Eucalyptus and
741 Spruce samples. A lower exponent of -1.4 for Spruce, compared to -2.0 for Eucalyptus, will have
742 no overlapping and interpenetrating conformations in the amorphous biopolymers, which results
743 in reduced constraints in maintaining order in the cellulose microfibril arrangement after
744 delignification. On the other hand, random flexible conformations which represents overlapping
745 and interpenetrating conformation as observed in Eucalyptus will still contribute to maintaining
746 order in the cellulose microfibril arrangement even after delignification. These holocellulose
747 samples with varying lignin content after the delignification process, and with retained
748 hemicellulose content and distinct hemicellulose populations in terms of glucomannan and xylan
749 depending on the source, represent valuable substrates to investigate the distinct effect of the
750 different loosening agents in disrupting non-covalent interactions between the cellulose microfibrils and
751 the different matrix polysaccharides.

752

753

754

755

756 **Table 3.** Fitting parameters extracted from the meridional SANS data analysis.

Sample	Sphere		Power-Law Exponent	
	Volume Fraction	R_{sph} (Å)	P2	P3
Q range (Å ⁻¹)	0.075 – 0.4		0.01 – 0.075	0.003 – 0.01
Eu_native	0.004 ± 0.002	9.3 ± 2.2	2.1 ± 0.1	4.2 ± 0.2
Eu_HC	0.009 ± 0.003	12.4 ± 0.2	2.0 ± 0.2	4.0 ± 0.2
Eu_PcaLOOL12	0.011 ± 0.002	12.3 ± 0.1	2.2 ± 0.1	4.1 ± 0.1
Eu_PcaLOOL7	0.009 ± 0.003	12.4 ± 0.1	2.1 ± 0.1	4.1 ± 0.1
Eu_PcaLOOL9	0.007 ± 0.003	12.3 ± 0.1	2.0 ± 0.2	4.0 ± 0.1
Sp_native	0.008 ± 0.002	11.9 ± 1.0	1.4 ± 0.2	3.9 ± 0.2
Sp_HC	0.008 ± 0.002	19.7 ± 0.1	1.3 ± 0.3	4.0 ± 0.2
Sp_PcaLOOL12	0.003 ± 0.001	18.1 ± 0.1	1.4 ± 0.1	4.0 ± 0.1
Sp_PcaLOOL7	0.005 ± 0.003	18.6 ± 0.1	1.4 ± 0.1	4.1 ± 0.1
Sp_PcaLOOL9	0.003 ± 0.001	19.4 ± 0.1	1.4 ± 0.1	4.0 ± 0.1

757 Eu: Eucalyptus; Sp: Spruce; HC: holocellulose

758

759

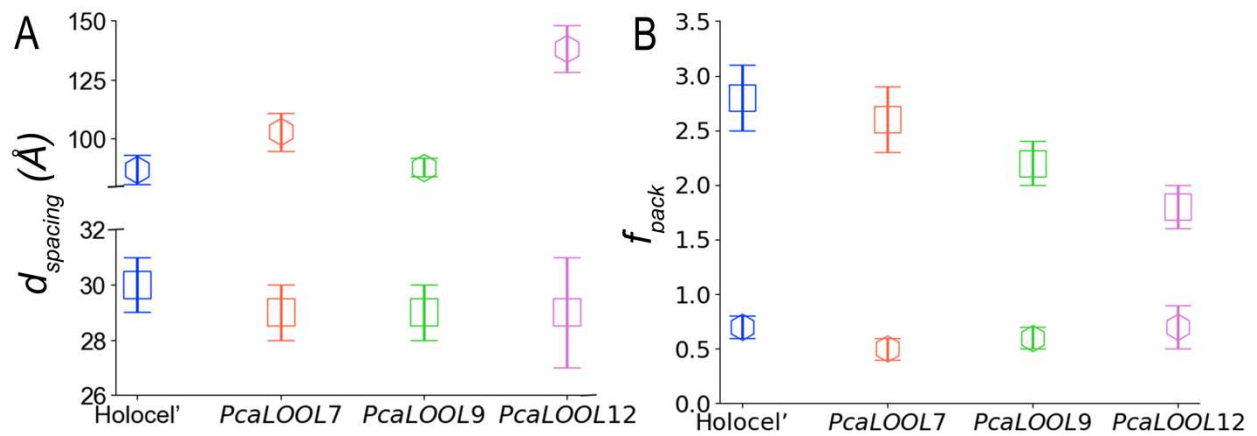
760 **Effect of PcaLOOLs on native wood and holocellulose samples.** The 1D equatorial SANS
761 profiles of Eucalyptus and Spruce holocellulose samples after 24 h reaction with different
762 PcaLOOL proteins are shown in Figure 5. Quantitative structural information extracted from the
763 fitted data (Table 2) revealed no change to the microfibril cross-sectional radius after treatment
764 with PcaLOOLs, indicating the proteins do not induce detectable fiber swelling. Instead,
765 PcaLOOLs impacted the inter-microfibril distance ($d_{spacing}$) and the packing parameter (f_{pack}) of
766 holocelluloses in a substrate-dependent manner (Figure 7).

767

768 Specifically, *PcaLOOL12* increased the $d_{spacing}$ in Spruce holocellulose by 59%, from $87 \pm 6 \text{ \AA}$
 769 to $138 \pm 10 \text{ \AA}$, and *PcaLOOL7* increased the $d_{spacing}$ by 18%, from $87 \pm 6 \text{ \AA}$ to $103 \pm 8 \text{ \AA}$ (Figure
 770 7A, Table 2). Although *PcaLOOL* treatment did not impact $d_{spacing}$ in Eucalyptus holocellulose,
 771 *PcaLOOL12* reduced the f_{pack} for Eucalyptus holocellulose by 36% from 2.8 ± 0.3 to 1.8 ± 0.2 ,
 772 and *PcaLOOL9* reduced the f_{pack} by 21% from 2.8 ± 0.3 to 2.2 ± 0.2 (Figure 7B, Table 2).

773

774



775

776 **Figure 7.** Inter-microfibril distance (A) and packing parameter (B) obtained from fitting the
 777 Eucalyptus (open squares) and the Spruce (open hexagons) data.

778

779 The meridional scattering profiles for the series of samples treated with *PcaLOOLs* showed no
 780 change, implying that *PcaLOOLs* mainly affected the regular arrangement of the cellulose
 781 microfibrils and not the cross-sectional radius of the cellulose microfibrils, micron-sized large
 782 structures, or the matrix co-polymer organization (Table 3, Figure 6).

783

784 The impact of *PcaLOOL12*, and to a lesser extent *PcaLOOL7*, on the $d_{spacing}$ of Spruce
 785 holocellulose but not Eucalyptus holocellulose correlates to the larger impact that delignification
 786 alone had on the $d_{spacing}$ of Spruce microfibrils (Table 2). Since the lignin is expected to largely

787 localize to the outer parts of microfibrils, the reorganization of hemicelluloses
788 (galactoglucomannan) upon the delignification of Spruce could have induced the observed
789 increase in $d_{spacing}$ of microfibrils, which could increase *PcaLOOL12* access to targeted regions
790 within the microfibrils. Delignification had a comparatively low impact on the inter-fibril
791 spacing ($d_{spacing}$) of Eucalyptus microfibrils (Table 2). A compelling possibility, then, is that the
792 decrease in f_{pack} observed when treating Eucalyptus holocellulose with *PcaLOOL12*, and to a
793 lesser extent *PcaLOOL9*, might precede protein-mediated impacts to $d_{spacing}$. Evaluating the
794 impact of time and protein load would address this possibility. The greatest impact of
795 *PcaLOOL12* on holocellulose samples compared to other *PcaLOOLs* is intriguing and yet
796 consistent with earlier studies that show comparatively high impacts of *PcaLOOL12* on cellulose
797 filter paper weakening and boosting of cellulolytic enzymes on lignocellulose (21,27). Notably,
798 early transcriptomic studies of *P. carnosus* showed highest transcript abundance for *PcaLOOL12*
799 over all other loosening proteins encoded by the source organism, suggesting a comparatively important
800 biological function for *PcaLOOL12* (15). Moreover, *PcaLOOL12* was assigned to a different
801 phylogenetic subgroup than *PcaLOOL7* and *PcaLOOL9* (15), has a comparatively low predicted
802 surface charge (27), and herein was observed to adopt the most compact protein conformation
803 which could enhance its accessibility to targeted positions within cellulose substrates.

804

805 **CONCLUSIONS**

806 Microbial expansin-related proteins, including loosening proteins, constitute a compelling protein family
807 for opening up cellulose fiber networks to enable fiber dissolution or enzymatic treatments that
808 lead to fiber surface modification or deconstruction. While this protein family is thought to act at
809 tight junctions between neighboring cellulose microfibrils or between cellulose microfibrils and

810 matrix polysaccharides, studies to date have been somewhat conflicted concerning impacts of the
811 protein action on fiber swelling versus fibrillation. Herein, SANS was used to study the impact
812 of loosensins from *P.carnososa* (*PcaLOOL7*, *PcaLOOL9*, and *PcaLOOL12*) on the organization of
813 cellulose microfibrils in hardwood (Eucalyptus) and softwood (Spruce) following their partial
814 delignification. *PcaLOOL12* treatment led to greatest impacts on both Eucalyptus and Spruce
815 samples, leading to a decrease in packing organization and increase in interfibril distance,
816 respectively. Notably, compared to Eucalyptus, the delignification of the Spruce sample
817 substantially reduced the packing organization of corresponding microfibrils prior to *PcaLOOL*
818 treatment, likely due to differences in the corresponding type and content of hemicelluloses.
819 Accordingly, the differences in impacts of *PcaLOOL12* on these materials, suggests a
820 progression of protein action from reducing microfibril packing order to increasing interfibril
821 spacing. Critically, the microfibril radii were unchanged after *PcaLOOL* treatment, indicating
822 the proteins induce fiber fibrillation over microfibril swelling; however, the possibility that
823 microfibril swelling would be observed over time cannot be ruled out. The progression of
824 *PcaLOOL* action on the holocellulose samples could be addressed through SANS studies that
825 investigate impact of *PcaLOOL12* dose and incubation time on the microfibril organization.
826

827 Structural characterization of the *PcaLOOLs* points to their functioning as monomeric proteins.
828 In particular, the NMR analysis of *PcaLOOL12* reveals the first solved structure of a loosenin
829 protein, and thereby, significantly augments the small number of expansin-related protein
830 structures currently available. The NMR structure shows the N-terminal insertion of
831 *PcaLOOL12* is located distal to the polysaccharide binding groove, and so it is difficult to see
832 how the insertion could directly impact substrate interactions. Alternatively, it is conceivable that

833 the sequence insertion in *PcaLOOL7* and *PcaLOOL9*, which is lacking from *PcaLOOL12* and
834 shows potential to fold into or extend the predicted polysaccharide binding groove, could have
835 limited their action on the holocelluloses tested herein. Structures of these subgroup A
836 *PcaLOOLs* will help to examine this prediction, and combined with a broader analysis of
837 loosenin model structures, will shed additional light on sequence and structural determinants of
838 substrate preference within the expansin-related protein family.

839

840 REFERENCES

841

- 842 1. Cosgrove DJ. Characterization of long-term extension of isolated cell walls from growing
843 cucumber hypocotyls. *Planta*. 1989;177(1):121-30.
- 844 2. Cosgrove DJ. Plant expansins: Diversity and interactions with plant cell walls. *Curr Opin*
845 *Plant Biol*. 2015; 25: 162–72.
- 846 3. McQueen-Mason S, Durachko DM, Cosgrove DJ. Two endogenous proteins that induce
847 cell wall extension in Plants. *Plant Cell*. 1992; 4(11):1425.
- 848 4. Cosgrove D. Structure and growth of plant cell walls. *Nat Rev Mol Cell Biol*. 2023;1–19.
- 849 5. Park Y, Cosgrove D. A revised architecture of primary cell walls based on biomechanical
850 changes induced by substrate-specific endoglucanases. *Plant Physiol*. 2012;158(4):1933–
851 43.
- 852 6. Sampedro J, Cosgrove DJ. The expansin superfamily. *Genome Biol*. 2005; 6(12):1–11.
- 853 7. Georgelis N, Nikolaidis N, Cosgrove DJ. Bacterial expansins and related proteins from the
854 world of microbes. *Appl Microbiol Biotechnol*. 2015; 99(9):3807–23.
- 855 8. Cosgrove DJ. Microbial Expansins. *Annu Rev Microbiol*. 2017; 71:479–97.
- 856 9. Chase WR, Zhaxybayeva O, Rocha J, Cosgrove DJ, Shapiro LR. Global cellulose
857 biomass, horizontal gene transfers and domain fusions drive microbial expansin evolution.
858 *New Phytol*. 2020;226(3):921-938.

- 859 10. Kerff F, Amoroso A, Herman R, Sauvage E, phanie Petrella S, Filé P, et al. Crystal
860 structure and activity of *Bacillus subtilis* YoaJ (EXLX1), a bacterial expansin that
861 promotes root colonization. *Biochem.* 2008;105 ((44):16876–81.
- 862 11. Georgelis N, Tabuchi A, Nikolaidis N, Cosgrove DJ. Structure-function analysis of the
863 bacterial eexpansin EXLX1. *J. Biol Chem.* 2011;286(19):16814–23.
- 864 12. Hepler NK, Cosgrove DJ. Directed in vitro evolution of bacterial expansin BsEXLX1 for
865 higher cellulose binding and its consequences for plant cell wall-loosening activities.
866 *FEBS Lett.* 2019;593(18):2545–55.
- 867 13. Saloheimo M, Paloheimo M, Hakola S, Pere J, Swanson B, Nyysönen E, Bhatia A, Ward
868 M, Penttilä M. Swollenin, a *Trichoderma reesei* protein with sequence similarity to the
869 plant expansins, exhibits disruption activity on cellulosic materials. *Eur J Biochem.* 2002;
870 269(17):4202-11.
- 871 14. Quiroz-Castañeda RE, Martínez-Anaya C, Cuervo-Soto LI, Segovia L, Folch-Mallol JL.
872 Loosenin, a novel protein with cellulose-disrupting activity from *Bjerkandera adusta*.
873 *Microb Cell Fact.* 2011;10:8.
- 874 15. Suzuki H, Vuong TV, Gong Y, Chan K, Ho CY, Master ER, Kondo A. Sequence diversity
875 and gene expression analyses of expansin-related proteins in the white-rot basidiomycete,
876 *Phanerochaete carnososa*. *Fungal Genet Biol.* 2014;72:115-123.
- 877 16. Andberg M, Penttilä M, Saloheimo M. Swollenin from *Trichoderma reesei* exhibits
878 hydrolytic activity against cellulosic substrates with features of both endoglucanases and
879 cellobiohydrolases. *Bioresour Technol.* 2015;181:105–13.
- 880 17. Kim I, Lee H, Choi I, Kim K. Synergistic proteins for the enhanced enzymatic hydrolysis
881 of cellulose by cellulase. *Appl Microbiol Biotechnol.* 2014;98:8469–80.
- 882 18. Gourlay K, Hu J, Arantes V, Andberg M, Saloheimo M, Penttilä M, Saddler J. Swollenin
883 aids in the amorphogenesis step during the enzymatic hydrolysis of pretreated biomass.
884 *Bioresour Technol.* 2013;142:498-503.
- 885 19. Bunternngsook B, Eurwilaichitr L, Thamchaipenet A, Champreda V. Binding
886 characteristics and synergistic effects of bacterial expansins on cellulosic and
887 hemicellulosic substrates. *Bioresour Technol.* 2014;176:129–35.

- 888 20. Ding S, Liu X, Hakulinen N, Taherzadeh M, Wang Y, Wang Y, et al. Boosting enzymatic
889 degradation of cellulose using a fungal expansin: Structural insight into the pretreatment
890 mechanism. *Bioresour Technol.* 2022;358:127434.
- 891 21. Dahiya D, Koitto T, Kutvonen K, Wang Y, Momeni M, de Ruijter S, et al. Fungal
892 loosenin-like proteins boost the cellulolytic enzyme conversion of pretreated wood fiber
893 and cellulosic pulps. *Bioresour Technol.* 2024;394:130188.
- 894 22. Baker JO, King MR, Adney WS, Decker SR, Vinzant TB, Lantz SE, et al. Investigation of
895 the cell-wall loosening protein expansin as a possible additive in the enzymatic
896 saccharification of lignocellulosic biomass. *Appl Biochem Biotechnol.* 2000;84-86:217-
897 23.
- 898 23. Liu X, Ma Y, Zhang M. Research advances in expansins and expansion-like proteins
899 involved in lignocellulose degradation. *Biotechnol Lett.* 2015;37(8):1541–51.
- 900 24. Eibinger M, Sigl K, Sattelkow J, Ganner T, Ramoni J, Seiboth B, et al. Functional
901 characterization of the native swollenin from *Trichoderma reesei*: Study of its possible
902 role as C1 factor of enzymatic lignocellulose conversion. *Biotechnol Biofuels.* 2016;
903 9(1):178
- 904 25. Lee H, Lee S, Ko H, Kim K, Choi I. An expansin-like protein from *Hahella chejuensis*
905 binds cellulose and enhances cellulase activity. *Mol Cells.* 2010;29(4):379–85.
- 906 26. Olarte-Lozano M, Mendoza-Nuñez MA, Pastor N, Segovia L, Folch-Mallol J, Martínez-
907 Anaya C. PcEx11 a novel acid expansin-like protein from the plant pathogen
908 *Pectobacterium carotovorum*, binds cell walls differently to BsEXLX1. *PLoS One.* 2014;
909 9(4):e95638.
- 910 27. Monschein M, Ioannou E, Koitto T, Al Amin LAKM, Varis JJ, Wagner ER, et al.
911 Loosenin-like proteins from *Phanerochaete carnosae* impact both cellulose and chitin fiber
912 networks . *Appl Environ Microbiol.* 2023; 89(1):e0186322.
- 913 28. Curtis JE, Nanda H, Khodadadi S, Cicerone M, Lee HJ, McAuley A, et al. Small-angle
914 neutron scattering study of protein crowding in liquid and solid phases: Lysozyme in
915 aqueous solution, frozen solution, and carbohydrate powders. *J Phys Chem B.*
916 2012;116(32):9653–67.

- 917 29. Pingali SV, Urban VS, Heller WT, McGaughey J, O'Neill HM, Foston M, et al. SANS
918 study of cellulose extracted from switchgrass. *Acta Crystallogr D Biol Crystallogr*. 2010;
919 66(11):1189–93.
- 920 30. Zhu Y, Plaza N, Kojima Y, Yoshida M, Zhang J, Jellison J, et al. Nanostructural analysis
921 of enzymatic and non-enzymatic brown rot fungal deconstruction of the lignocellulose cell
922 wall. *Front Microbiol*. 2020;11:551979.
- 923 31. Wise L, Murphy M, d'Addieco A. Chlorite holocellulose, its fractionation and bearing on
924 summative wood analysis and on studies on the hemicelluloses. *Pap Trade J*.
925 1946;122(2):35–43.
- 926 32. Ahlgren PA, Goring DAI. Removal of wood components during chlorite delignification of
927 black spruce. *Can J Chem*. 1971;49(8):1272–5.
- 928 33. Saeman J. Techniques for the determination of pulp constituents by quantitative paper
929 chromatography. *Tappi*. 1954;37:336–43.
- 930 34. Albersheim P, Nevins D, English P, Karr A. A method for the analysis of sugars in plant
931 cell-wall polysaccharides by gas-liquid chromatography. *Carbohydr Res*. 1967;5(3):340–
932 5.
- 933 35. Iiyama K, Wallis AFA. An improved acetyl bromide procedure for determining lignin in
934 woods and wood pulps. *Wood Sci Technol*. 1988;22(3):271–80.
- 935 36. Johnson D, Moore W, Zank L. The spectrophotometric determination of lignin in small
936 wood samples. *Tappi*. 1961;44(11):793.
- 937 37. Hatfield RD, Grabber J, Ralph J, Brei K. Using the acetyl bromide assay to determine
938 lignin concentrations in herbaceous plants: Some cautionary notes. *J Agric Food Chem*.
939 1999;47(2):628–32.
- 940 38. Correddu D, López JM, Vadakkedath P, Lai A, Pernes J, Watson P, et al. An improved
941 method for the heterologous production of soluble human ribosomal proteins in
942 *Escherichia coli*. *Sci Rep*. 2019;9(1):8884.
- 943 39. LaVallie E, Lu Z, Diblasio-Smith E, Collins-Racie L, McCoy J. Thioredoxin as a fusion
944 partner for production of soluble recombinant proteins in *Escherichia coli*. *Methods*
945 *Enzymol*. 2000;326(326):322–40.

- 946 40. Szyperski T, Yeh DC, Sukumaran DK, Moseley HNB, Montelione GT. Reduced-
947 dimensionality NMR spectroscopy for high-throughput protein resonance assignment.
948 Proc Natl Acad Sci U S A. 2002;99(12):8009–14.
- 949 41. Delaglio F, Grzesiek S, Vuister G, Zhu G, Pfeifer J, Bax A. NMRPipe: A
950 multidimensional spectral processing system based on UNIX pipes. J Biomol NMR.
951 1995;6(3):277–93.
- 952 42. Lee W, Rahimi M, Lee Y, Chiu A. POKY: a software suite for multidimensional NMR
953 and 3D structure calculation of biomolecules. Bioinformatics. 2021;37(18):3041–2.
- 954 43. Güntert P. Automated NMR structure calculation with CYANA. Methods Mol Biol..
955 2004;278:353–78.
- 956 44. Shen Y, Delaglio F, Cornilescu G, Bax A. TALOS+: A hybrid method for predicting
957 protein backbone torsion angles from NMR chemical shifts. J Biomol NMR.
958 2009;44:213–23.
- 959 45. Sharma D, Rajarathnam K. ¹³C NMR chemical shifts can predict disulfide bond
960 formation. J Biomol NMR. 2000;18(2):165–71.
- 961 46. Linge JP, Williams MA, Spronk CAEM, Bonvin AMJJ, Nilges M. Refinement of protein
962 structures in explicit solvent. Proteins. 2003; 50(3):496-506.
- 963 47. Bhattacharya A, Tejero R, Montelione G. Evaluating protein structures determined by
964 structural genomics consortia. Proteins. 2007;66(4):778–95.
- 965 48. Difabio J, Chodankar S, Pjerov S, Jakoncic J, Lucas M, Krywka C, et al. The life science
966 x-ray scattering beamline at NSLS-II. AIP Conf Proc. 2016;1741(1): 030049.
- 967 49. Yang L, Antonelli S, Chodankar S, Byrnes J, Lazo E, Qian K. Solution scattering at the
968 Life Science X-ray Scattering (LiX) beamline. J Synchrotron Radiat. 2020;27(3):804–12.
- 969 50. Yang L, Lazo E, Byrnes J, Chodankar S, Antonelli S, Rakin M. Tools for supporting
970 solution scattering during the COVID-19 pandemic. J Synchrotron Radiat.
971 2021;28(4):1237–44.
- 972 51. Hopkins J, Gillilan R, Skou S. BioXTAS RAW: improvements to a free open-source
973 program for small-angle X-ray scattering data reduction and analysis. J Appl Crystallogr.
974 2017;50(5):1545–53.

- 975 52. Franke D, Petoukhov M, Konarev P, Panjkovich A, Tuukkanen A, Mertens H, et al.
976 ATASAS 2.8: a comprehensive data analysis suite for small-angle scattering from
977 macromolecular solutions. *J Appl Crystallogr.* 2017;50(4):1212–25.
- 978 53. Svergun D. Determination of the regularization parameter in indirect-transform methods
979 using perceptual criteria. *J Appl Crystallogr.* 1992;25(4):495–503.
- 980 54. Piiadov V, Ares de Araujo E, Oliveira Neto M, Craievich A, Polikarpov I. SAXSMoW 2.0
981 Online calculator of the molecular weight of proteins in dilute solution from experimental
982 SAXS data measured on a relative scale. *Protein Sci.* 2019;28(2):454–63.
- 983 55. Schneidman-Duhovny D, Hammel M, Sali A. FoXS: a web server for rapid computation
984 and fitting of SAXS profiles. *Nucleic Acids Res.* 2010;38(2):W540–4.
- 985 56. Schneidman-Duhovny D, Hammel M, Tainer J, Sali A. Accurate SAXS profile
986 computation and its assessment by contrast variation experiments. *Biophys J.*
987 2013;105(4):962–74.
- 988 57. Jumper J, Evans R, Pritzel A, Green T, Figurnov M, Ronneberger O, et al. Highly accurate
989 protein structure prediction with AlphaFold. *Nature.* 2021;596:583–9.
- 990 58. Pettersen EF, Goddard TD, Huang CC, Couch GS, Greenblatt DM, Meng EC, et al. UCSF
991 Chimera—a visualization system for exploratory research and analysis. *J Comput Chem.*
992 2004;25(13):1605–12.
- 993 59. Senanayake M, Lin CY, Mansfield SD, Eudes A, Davison BH, Pingali SV, et al. Ectopic
994 production of 3,4-dihydroxybenzoate in planta affects cellulose structure and organization.
995 *Biomacromolecules.* 2024; 25(6):3542-3553.
- 996 60. Ilavsky J, Jemian PR. Irena: Tool suite for modeling and analysis of small-angle
997 scattering. *J Appl Crystallogr.* 2009;42(2):347–53.
- 998 61. Beaucage G. Approximations leading to a unified exponential/power-law approach to
999 small-angle scattering. *J Appl Crystallogr.* 1995;28(6):717–28.
- 1000 62. Mark J, Lee C, Bianconi P. Hybrid Organic-inorganic composites. PA Bianconi, Eds.
1001 1994.
- 1002 63. Yee A, Chang X, Pineda-Lucena A, Wu B, Semesi A, Le B, et al. An NMR approach to
1003 structural proteomics. *Proc Natl Acad Sci U S A.* 2002; 99(4):1825–30.
- 1004 64. Rossi P, Swapna G, Huang Y, Aramini J, Anklin C, Conover K, et al. A microscale
1005 protein NMR sample screening pipeline. *J Biomol NMR.* 2010;46(1):11–22.

- 1006 65. Castillo R, Mizuguchi K, Dhanaraj V, Albert A, Blundell T, Murzin A. A six-stranded
1007 double-psi β barrel is shared by several protein superfamilies. *Structure*. 1999;7(2):227–
1008 36.
- 1009 66. Wu R, Smith C, Buchko G, Blaby I, Paez-Espino D, Kyripides N, et al. Structural
1010 characterization of a soil viral auxiliary metabolic gene product—a functional chitosanase.
1011 *Nat Commun*. 2022;13(1):5485.
- 1012 67. Holm L. DALI and the persistence of protein shape. *Protein Sci*. 2020;29(1):128–40.
- 1013 68. Juettner N, Schmelz S, Bogen J, Happel D, Fessner W, Pfeifer F, et al. Illuminating
1014 structure and acyl donor sites of a physiological transglutaminase substrate from
1015 *Streptomyces mobaraensis*. *Protein Sci*. 2018;27(5):910–22.
- 1016 69. Moynie L, Schnell R, McMahon S, Sandalova T, Boulkerou W, Schmidberger J, et al. The
1017 AEROPATH project targeting *Pseudomonas aeruginosa*: crystallographic studies for
1018 assessment of potential targets in early-stage drug discovery. *Acta Crystallogr Sect F*
1019 *Struct Biol Cryst Commun*. 2013;69(1):25–34.
- 1020 70. Offermann LR, Giangrieco I, Perdue ML, Zuzzi S, Santoro M, Tamburrini M, et al.
1021 Elusive structural, functional, and immunological features of Act d 5, the Green Kiwifruit
1022 Kiwellin. *J Agric Food Chem*. 2015;63(29):6567–76.
- 1023 71. Ciardiello M, Giangrieco I, Tuppo L, Tamburrini M, Buccheri M, Palazzo P, et al.
1024 Influence of the natural ripening stage, cold storage, and ethylene treatment on the protein
1025 and IgE-binding profiles of green and gold kiwi fruit extracts. *J Agric Food Chem*.
1026 2009;57(4):1565–71.
- 1027 72. Sarafeddinov A, Arif A, Peters A, Fuchsbauer H. A novel transglutaminase substrate from
1028 *Streptomyces mobaraensis* inhibiting papain-like cysteine proteases. *J Microbiol*
1029 *Biotechnol*. 2011;21(6):617–26.
- 1030 73. Bhardwaj G, Mulligan V, Bahl C, Gilmore J, Harvey P, Cheneval O, et al. Accurate de
1031 novo design of hyperstable constrained peptides. *Nature*. 2016;538(7625):329–35.
- 1032 74. Chen P, Li Y, Nishiyama Y, Pingali SV, O'Neill HM, Zhang Q, et al. Small-angle neutron
1033 scattering shows nanoscale PMMA distribution in transparent wood biocomposites. *Nano*
1034 *Lett*. 2021;21(7):2883–90.

- 1035 75. Penttilä PA, Altgen M, Carl N, van der Linden P, Morfin I, Österberg M, et al. Moisture-
1036 related changes in the nanostructure of woods studied with x-ray and neutron scattering.
1037 Cellulose. 2020;27(1):71–87.
- 1038 76. Saxe F, Eder M, Benecke G, Aichmayer B, Fratzl P, Burgert I, et al. Measuring the
1039 distribution of cellulose microfibril angles in primary cell walls by small-angle x-ray
1040 scattering. Plant Methods. 2014;10(1):25.
- 1041 77. Fernandes AN, Thomas LH, Altaner CM, Callow P, Forsyth VT, Apperley DC, et al.
1042 Nanostructure of cellulose microfibrils in spruce wood. Proc Natl Acad Sci U S A.
1043 2011;108(47):E1195-203.
- 1044 78. Thomas L, Martel A, Grillo I, Jarvis M. Hemicellulose binding and the spacing of
1045 cellulose microfibrils in spruce wood. Cellulose. 2020;27(8):4249–54.
- 1046 79. Nishiyama Y, Langan P, O’Neill H, Pingali S, Harton S. Structural coarsening of aspen
1047 wood by hydrothermal pretreatment monitored by small- and wide-angle scattering of x-
1048 rays and neutrons on oriented specimens. Cellulose. 2014; 21(2):1015–24.
- 1049 80. Dupree R, Simmons TJ, Mortimer JC, Patel D, Iuga D, Brown SP, et al. Probing the
1050 molecular architecture of *Arabidopsis thaliana* secondary cell walls using two- and three-
1051 dimensional ¹³C solid state nuclear magnetic resonance. Biochem. 2015;54(14):2335–45.
- 1052 81. Simmons T, Mortimer J, Bernardinelli O, Pöpler AC, Brown SP, Deazevedo ER, et al.
1053 Folding of xylan onto cellulose fibrils in plant cell walls revealed by solid-state NMR. Nat
1054 Commun. 2016;7(1):13902.
- 1055 82. Shatalov A, Evtuguin D, Neto C. (2-O- α -d-Galactopyranosyl-4-O-methyl- α -d-glucurono)-
1056 d-xylan from *Eucalyptus globulus* Labill. Carbohydr Res. 1999;320(1–2):93–9.
- 1057 83. Terrett O, Dupree P. Covalent interactions between lignin and hemicelluloses in plant
1058 secondary cell walls. Curr Opin Biotechnol. 2019;56:97–104.
- 1059 84. Martínez-Abad A, Jiménez-Quero A, Wohlert J, Vilaplana F. Influence of the molecular
1060 motifs of mannan and xylan populations on their recalcitrance and organization in spruce
1061 softwoods. Green Chem. 2020;22(12):3956–70.
- 1062 85. Lyczakowski J, Bourdon M, Terrett O, Helariutta Y, Wightman R, Dupree P. Structural
1063 imaging of native cryo-preserved secondary cell walls reveals the presence of macrofibrils
1064 and their formation requires normal cellulose, lignin and xylan biosynthesis. Front Plant
1065 Sci. 2019;10:1398.

1066 86. Beaucage G. Small-angle scattering from polymeric mass fractals of arbitrary mass-fractal
1067 dimension. J Appl Crystallogr. 1996;29(2):134–46.

1068

1069

1070 **LIST OF ABBREVIATIONS**

1071 LOOL: Loosenin-like proteins

1072 EXLX1: microbial expansin-like proteins

1073 SANS: small-angle neutron scattering

1074 SEC SAXS: size exclusion chromatography small-angle x-ray scattering

1075 WAXS: wide angle x-ray scattering

1076 NMR: nuclear magnetic resonance

1077 NOESY-HSQC: Nuclear Overhauser Effect Spectroscopy - Heteronuclear single quantum

1078 coherence

1079 NMA: Normal Mode Analysis

1080 HPAEC-PAD high-performance anion-exchange chromatography coupled with pulsed amper:

1081 metric detection

1082

1083 **ACKNOWLEDGMENTS**

1084 We acknowledge all scientific discussions enabled through the BioUPGRADE research network

1085 (<https://biouppgrade.eu>).

1086

1087 **FUNDING**

1088 This project has received funding from the European Union’s Horizon 2020 research and

1089 innovation programme under grant agreement No 964764. The content presented in this

1090 document represents the views of the authors, and the Commission is not responsible for any use
1091 that may be made of the information it contains. This research was also performed on project
1092 award 60859 under the FICUS program
1093 (<https://dx.doi.org/10.46936/fics.proj.2023.60859/60008908>) and used resources at the DOE
1094 Environmental Molecular Sciences Laboratory, which are DOE Office of Science User
1095 Facilities. The facility is sponsored by the Biological and Environmental Research program and
1096 operated under Contract No. DE-AC05-76RL01830 (EMSL). The scattering portion of this work
1097 further acknowledges the support of the Genomic Science Program, under Contract FWP
1098 ERKP752 and the Center for Structural Molecular Biology (CSMB) under Contract FWP
1099 ERKP291, Office of Biological and Environmental Research, U.S. Department of Energy and
1100 the High Flux Isotope Reactor supported by the Basic Energy Sciences, U.S. Department of
1101 Energy. The LiX beamline is part of the Center for BioMolecular Structure (CBMS), which is
1102 primarily supported by the National Institutes of Health, National Institute of General Medical
1103 Sciences (NIGMS) through a P30 Grant (P30GM133893), and by the DOE Office of Biological
1104 and Environmental Research (KP1605010). LiX also received additional support from NIH
1105 Grant S10 OD012331. As part of NSLS-II, a national user facility at Brookhaven National
1106 Laboratory, work performed at the CBMS is supported in part by the U.S. Department of
1107 Energy, Office of Science, Office of Basic Energy Sciences Program under contract number DE-
1108 SC0012704. This manuscript has been coauthored by UT-Battelle, LLC, under Contract No. DE-
1109 AC05- 00OR22725 with the U.S. Department of Energy. The United States Government retains
1110 and the publisher, by accepting the article for publication, acknowledges that the United States
1111 Government retains a non-exclusive, paid-up, irrevocable, worldwide license to publish or

1112 reproduce the published form of this manuscript or allow others to do so, for United States
1113 Government purposes.

1114

1115 **CONTRIBUTIONS**

1116 DD, HMO and ERM, together with ZPS, FV and SVP conceived the research plan and designed
1117 the experiments. DD produced the proteins in *Pichia pastoris* and ZPS together with PS prepared
1118 the holocellulose samples. MS, SVP and HMO conducted the SANS experiments and together
1119 with DD, ZPS, ERM and FV, interpreted the results. WL constructed the *PcaLOOL* model
1120 structures and together with and JB performed the SEC-SAXS analyses. GWB produced
1121 *PcaLOOL12* in *Escherichia coli* and solved the *PcaLOO12* NMR solution structure. DD, HMO
1122 and ERM drafted the manuscript with major contributions from all co-authors. All authors
1123 reviewed and finalized the manuscript.

1124

1125 **ETHICS DECLARATION**

1126 **Ethics approval and consent to participate.**

1127 Not applicable.

1128

1129 **CONSENT FOR PUBLICATION**

1130 Not applicable.

1131

1132 **COMPETING INTERESTS**

1133 The authors certify that there is no competing of interest.

1134

Supplementary Files

This is a list of supplementary files associated with this preprint. Click to download.

- [DahiyaSupplMaterialssubmitted18July2024.pdf](#)